

COMPUTER VISION BASED
EARLY INTRAOCULAR PRESSURE ASSESSMENT
FROM FRONTAL EYE IMAGES

Mohammad Atallah Al-Oudat

Under the Supervision of Dr. Miad Faezipour

DISSERTATION

SUBMITTED IN PARTIAL FULFILMENT OF THE REQUIREMENTS
FOR THE DEGREE OF DOCTOR OF PHILOSOPHY IN COMPUTER SCIENCE

AND ENGINEERING

THE SCHOOL OF ENGINEERING

UNIVERSITY OF BRIDGEPORT

CONNECTICUT

December, 2018


COMPUTER VISION BASED EARLY INTRAOCULAR
PRESSURE ASSESSMENT FROM FRONTAL EYE IMAGES

Mohammad Atallah Moh'd Al-Oudat

Under the Supervision of Dr. Miad Faezipour

Approvals

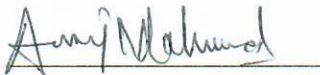
Committee Members

Name	Signature	Date
Dr. Miad Faezipour		<u>Dec 7, 2018</u>
Dr. Prabir Patra		<u>Dec 10, 2018</u>
Dr. Xingguo (Michael) Xiong		<u>Dec 7, 2018</u>
Dr. Buket D. Barkana		<u>12/11/2018</u>
Dr. Saeid Moslehpour		<u>Dec 16, 18</u>

Ph.D. Program Coordinator

Dr. Khaled M. Elleithy		<u>12/12/18</u>
------------------------	--	-----------------

Chairman, Computer Science and Engineering Department

Dr. Ausif Mahmood		<u>12-12-2018</u>
-------------------	--	-------------------

Dean, School of Engineering

Dr. Tarek M. Sobh		<u>12-19-2018</u>
-------------------	--	-------------------

COMPUTER VISION BASED EARLY INTRAOCULAR
PRESSURE ASSESSMENT FROM FRONTAL EYE IMAGES

© Copyright by Mohammad Atallah Al-Oudat 2018

COMPUTER VISION BASED EARLY INTRAOCULAR PRESSURE ASSESSMENT FROM FRONTAL EYE IMAGES

ABSTRACT

Intraocular Pressure (IOP) in general, refers to the pressure in the eyes. Gradual increase of IOP and high IOP are conditions or symptoms that may lead to certain diseases such as glaucoma, and therefore, must be closely monitored. While the pressure in the eye increases, different parts of the eye may become affected until the eye parts are damaged. An effective way to prevent rise in eye pressure is by early detection. Existing IOP monitoring tools include eye tests at clinical facilities and computer-aided techniques from fundus and optic nerves images. In this work, a new computer vision-based smart healthcare framework is presented to evaluate the intraocular pressure risk from frontal eye images early-on. The framework determines the status of IOP by analyzing frontal eye images using image processing and machine learning techniques. A database of images from the Princess Basma Hospital was used in this work. The database contains 400 eye images; 200 images with normal IOP and 200 high eye pressure case images. This study proposes novel features for IOP determination from two experiments. The first experiment extracts the sclera using circular hough transform, after which four features are extracted from the whole sclera.

These features are mean redness level, red area percentage, contour area and contour height. The pupil/iris diameter ratio feature is also extracted from the frontal eye image after a series of pre-processing techniques. The second experiment extracts the sclera and iris segment using a fully conventional neural network technique, after which six features are extracted from only part of the segmented sclera and iris. The features include mean redness level, red area percentage, contour area, contour distance and contour angle along with the pupil/iris diameter ratio. Once the features are extracted, classification techniques are applied in order to train and test the images and features to obtain the status of the patients in terms of eye pressure. For the first experiment, neural network and support vector machine algorithms were adopted in order to detect the status of intraocular pressure. The second experiment adopted support vector machine and decision tree algorithms to detect the status of intraocular pressure. For both experiments, the framework detects the status of IOP (normal or high IOP) with high accuracies. This computer vision-based approach produces evidence of the relationship between the extracted frontal eye image features and IOP, which has not been previously investigated through automated image processing and machine learning techniques from frontal eye images.

ACKNOWLEDGEMENTS

My thanks are wholly devoted to Allah who has helped me all the way to complete this work successfully. I owe a debt of gratitude to my family for understanding and encouragement.

I am honored that my work has been supervised by Dr. Miad Faezipour, who inspired me through my journey to complete this professional work. My words are not enough to express my appreciation for her insight and guidance throughout this entire dissertation process and research work. I have learned so much, and without her, this would not have been possible. Thank you for helping me to succeed and instilling in me the confidence that I am capable of doing anything I put my mind to.

Also, I would like to extend my gratitude to the members of my dissertation supervisory committee, Dr. Prabir Patra, Dr. Xingguo (Michael) Xiong, Dr. Buket D. Barkana and Dr. Saeid Moslehpour for their time and valuable comments that helped me improve the quality of this dissertation.

Finally, I would like to thank my family, especially my parents and my wife for their unconditional support.

TABLE OF CONTENTS

ABSTRACT.....	iv
ACKNOWLEDGEMENTS.....	vi
TABLE OF CONTENTS.....	vii
LIST OF TABLES.....	x
LIST OF FIGURES.....	xii
CHAPTER 1: INTRODUCTION.....	1
1.1 Research Problem and Scope.....	3
1.2 Motivations.....	4
1.3 Contributions of the Proposed Research.....	6
CHAPTER 2: LITERATURE REVIEW.....	9
2.1 Related Work on Blood Vessels Detection.....	12
2.2 Related Work on Pupil/Iris Detection.....	17
2.3 Optic Nerve based on Fundus Images.....	18
2.4 Redness of the Sclera.....	19
2.5 Related Work on Mechanisms of Elevated Intraocular Pressure.....	19
2.6 Related Work on Optic Disc and Visual Field Changes.....	20
2.7 Related Work on Mechanism of Optic Nerve Damage.....	22
2.8 Related Work on Mechanical Considerations.....	22
2.9 Related Work on Vascular Considerations.....	24
CHAPTER 3: RESEARCH PLAN.....	26

3.1 Material (Database of Images).....	26
3.2 Method.....	27
3.3 Pre-Processing.....	28
3.4 First Experiment (Sclera segmentation using CHT).....	31
3.5 Second Experiment (Sclera segmentation using FCN).....	34
3.6 Feature Extraction.....	38
3.6.1 Pupil Iris Ratio.....	39
3.6.2 MRL.....	39
3.6.2.1 MRL - First Experiment - Whole Sclera.....	41
3.6.2.2 MRL - Second Experiment - Part of the Sclera.....	41
3.6.3 RAP.....	42
3.6.3.1 RAP - First Experiment - Whole Sclera.....	43
3.6.3.2 RAP - Second Experiment - Part of the Sclera.....	43
3.6.4 Sclera Contour Features.....	43
3.6.4.1 Contour Features (Area, Height) - First Experiment - Whole Sclera.....	43
3.6.4.2 Contour Features (Area, Distance, Angle) - Second Experiment.....	44
3.7 Feature Representation.....	48
3.7.1 Feature Representation for the First Experiment.....	49
3.7.2 Feature Representation for the second experiment.....	49
3.8 Classification.....	50
3.8.1 First Experiment.....	50
3.8.2 Second Experiment.....	51
CHAPTER 4: IMPLEMENTATION AND TEST PLAN.....	53
CHAPTER 5: RESULTS.....	55
5.1 First experiment.....	55

5.1.1 Pupil/Iris Ratio	55
5.1.2 MRL and RAP	56
5.1.3 Contour Features (Area, Height).....	56
5.1.4 High Risk IOP Determination.....	57
5.2 Second Experiment	61
5.2.1 Pupil/Iris Ratio	61
5.2.2 MRL and RAP	62
5.2.3 Contour Features (D, α , and Area).....	63
5.2.4 IOP Risk Determination.....	63
5.3 Statistical Power Analysis.....	69
5.4 Efficiency Test.....	72
CHAPTER 6: CONCLUSION AND FUTURE DIRECTIONS.....	75
REFERENCES	78

LIST OF TABLES

Table 1.1	Comparison with existing clinical methods	2
Table 2.1	Summary of related techniques	11
Table 3.1	Typical parameter values of Canny Edge, Gamma, Radius and Thresholding.	30
Table 3.2	Segmentation Metrics	36
Table 3.3	Ratio of Red Colors	40
Table 5.1	Test Confusion Matrix for neural network	59
Table 5.2	Test Confusion Matrix for SVM	59
Table 5.3	Test Confusion Matrix for neural network with three features (MRL, contour area, and contour height)	61
Table 5.4	Sample Values of Pupil/Iris Ratio, MRL, RAP and Contour features (Area, Height) Results for Normal, High Eye Pressure	61
Table 5.5	Sample of Pupil/Iris Ratio, MRL and RAP Feature Values for Normal and High IOP Cases	63
Table 5.6	Contour of the Sclera Feature Values for Normal	64

and High Intraocular Pressure Cases

Table 5.7	Training Phase Confusion Matrix for DT 65% of the data	67
Table 5.8	Validation Phase Confusion Matrix for DT 10% of the data	67
Table 5.9	Test Phase Confusion Matrix for DT 25% of the data	67
Table 5.10	Overall Confusion Matrix for DT 100% of the data	67
Table 5.11	Overall Confusion Matrix for SVM	67
Table 5.12	Cohen Table of Statistical Power Analysis	70

LIST OF FIGURES

Figure 1.1	General Depiction of the human eye.	6
Figure 3.1	IOP risk assessment framework. First experiment features: Pupil/Iris Ratio, MRL, RAP, Contour (Area, Height). Second Experiment: Pupil/Iris Ratio, MRL, RAP, Contour (Area, Distance and Angle). First experiment Classifiers: SVM, NN. Second Experiment Classifiers: SVM and DT.	28
Figure 3.2	Haar cascade classifier to detect object	29
Figure 3.3	Pre-processing stage to extract Iris and Pupil	29
Figure 3.4	Iris and Pupil detection using CHT technique	31
Figure 3.5	Extended eye image	31
Figure 3.6	Detecting Pupil/Iris and eyelids	32
Figure 3.7	Extracted sclera	33
Figure 3.8	Fully Convolutional Network (FCN) structure for sclera segmentation	35
Figure 3.9	Sclera and Iris segmentation (a) IOP Status; (b) Original Image; (c) FCN Result; (d) Hough transform Result; (e) Ground truth; (f) Masked Image from FCN	37
Figure 3.10	The Ratio of Pupil/Iris	39
Figure 3.11	Results of MRL and RAP for (a) Normal and (b) High IOP	41

Figure 3.12	Extracting sclera and calculating MRL/RAP features	42
Figure 3.13	Active contour	44
Figure 3.14	Depiction of Distance (d), Angle (α) and Area features of the contour of the sclera	46
Figure 3.15	Distance (D), Angle (α) and Area measurements	48
Figure 3.16	Features matrix For the First Experiment	49
Figure 3.17	Features matrix For the Second Experiment	49
Figure 4.1	MATLAB Software 2014a	54
Figure 4.2	Whole sclera extracted	54
Figure 4.3	Contour features adopted from sonar	55
Figure 4.4	MRL and RAP Region of Interest	55
Figure 5.1	Training and Testing Performance	60
Figure 5.2	The Constructed Decision Tree	66
Figure 5.3	(a) Normal eye pressure (b) High IOP	68
Figure 5.4	Correlation between normalized (a) Pupil/Iris Ratio feature,(b) Red Area Percentage feature, (c) Mean Redness Level feature,(d) Contour Distance feature, (e) Contour Area feature, and (f) Contour Angle feature, with IOP in mmHg.	69
Figure 5.5	(a) Red eye with Normal IOP (b) Cataract eye with Normal IOP	74

CHAPTER 1: INTRODUCTION

Rise of IOP is one of the most serious causes of glaucoma leading to blindness all over the world. It is known as the silent thief of vision because it can sneak up into any patient [1]. The blindness caused by IOP is irreversible as the optic nerve dies [2]. An effective way to prevent pressure rise inside the eye is through early detection. The earlier the disease is detected, the easier and more effective the treatment will be [3].

Initially, ophthalmologists label some patients as glaucoma candidates due to several risk factors and symptoms that their eyes may have. One of these factors is the suspicion of potential rise in IOP [4]. The pressure can increase inside the eye from a liquid called aqueous humor that is secreted by the ciliary body into the posterior chamber [5]. After that, the aqueous humor flows through the Pupil into the anterior chamber [6]. Finally, it drains through a sponge-like structure called the trabecular meshwork (TM) [7]. Moreover, the pressure damages the nerve fibers which can result in patches of vision loss, and if left untreated, may lead to total blindness. In addition, the rise of eye pressure will dilate the Pupil [8]. As the aqueous humor liquid builds up in the chamber, other factors can contribute to the onset of the rise of IOP through medications unrelated to eye disease. Different drugs that are taken for anxiety or depression affect the brain and physiological composition of the body [9]. This includes the muscles in the eye that control the Pupil size. The progression of IOP is generally preventable by

medical treatment, while some patients continue to progress even after treatment [10]. However, the portion of the vision that is already lost cannot be restored. That is why it is necessary to detect early signs of rise in IOP. Generally, regular eye exams like Tonometry test, Ophthalmo[scopy test, Perimetry test, Gonoscopy test, and Pachymetry test are conducted at the clinic for this purpose [11].

Table1.1 Comparison with existing clinical methods.

<i>Test Name</i>	<i>Eye Drops</i>	<i>Physical Contact</i>	<i>Examine/Measure</i>	<i>Clinic</i>
<i>Tonometry</i>	Must use	Yes, by using: 1. Air puff technique 2. Tonometry device	Pressure inside the eye Thickness of the cornea	Must be in clinic
<i>Ophthalmoscopy</i>	Must use to dilate the pupil	Yes	Shape and color of the Optic nerve	Must be in clinic
<i>Perimetry</i>	No	No	Visual field using LCD screen	Must be in clinic
<i>Gonoscopy</i>	Must use	Yes	Angle where the iris and cornea meet	Must be in clinic
<i>Pachymetry</i>	No	Yes	Thickness of the cornea	Must be in clinic
<i>Proposed work</i>	No	No physical contact	IOP Risk from frontal eye image features	Not needed (any room with lights on)

In this study, a new automated detection framework is developed to detect if the eye has normal or high eye pressure. Our smart framework is based on image processing and machine learning techniques to extract certain features, solely from the frontal eye image: the Pupil/Iris diameter or radius ratio, the Mean Redness Level (MRL) and Red Area Percentage (RAP) of the sclera, and features of the contour of the sclera. Table 1.1 shows a comparison between the existing clinical methods and the proposed framework. Once the features are extracted from the frontal eye images, classifiers such as neural network (NN), support vector machine (SVM) and decision tree (DT) are applied in order

to train and test the extracted images and features and to obtain a risk assessment result for intraocular pressure (normal or high IOP). The proposed work does not directly measure the IOP value in mmHg, rather it determines whether the user/patient's IOP is at a risky level (high) or not, further serving as an initial IOP risk assessment framework that can assist many individuals, especially those with family history of IOP and glaucoma to provide an early warning if their IOP is beyond the normal range. If the proposed initial screening framework resulted in high IOP, the patient must seek/visit the clinic/doctor for further examinations/consultations.

1.1 Research Problem and Scope

This research provides a computer vision-based initial diagnosis of potential rise of IOP from frontal eye images in (near) real-time. A direct simulation of this framework is applied to detect IOP early-on. The problem with IOP is that it takes a long time to affect the vision, so patients are unable to detect quickly that there is something wrong with the eye. In fact, half of the nerve is dead before the patients start to realize it. The only way to prevent IOP is by early detection. Therefore, it is important to study the nature of normal eye and compare it with eyes suffering from IOP from frontal eye images. This will lead us to compare the features between healthy and non-healthy eyes. The idea here is to introduce an initial IOP screening framework to monitor the status of IOP from frontal eye images. Early detection followed by proper actions taken by ophthalmologists is the only way to prevent the rise of IOP.

This work focuses on developing novel, efficient and feasible image-based techniques to i) extract the eye, ii) segment the eye sclera, iii) calculate the size of the iris and pupil, iii) measure the redness of the sclera, and iv) extract the sclera contour features. The ultimate goal is to have a developmental framework that associates the extracted features from the eye with the status of the IOP.

1.2 Motivations

Glaucoma is known as the silent blinding disease. It is one of the leading causes of blindness worldwide. Due to increased intraocular pressure (IOP), the optic nerve is damaged, vision is reduced, and the final result is Glaucoma [1]. As stated, the blindness caused by Glaucoma is irreversible as the optic nerve dies [2]. The only way to prevent blindness from Glaucoma is through early detection [3], because the earlier the disease is detected, the easier and more effective the treatment will be.

In an initial diagnosis, patients are referred to as Glaucoma candidates [4]. In most cases, this damage is found in candidates due to increased pressure within the eye. The eye produces a fluid called aqueous humor which is secreted by the ciliary body into the posterior chamber (a space between the Iris and the lens) [5]. Then, it flows through the Pupil into the anterior chamber between the Iris and the cornea [6]. From here, it drains through a sponge-like structure located at the base of the Iris called the trabecular meshwork [7], and then leaves the eye, as shown in Figure 1.1. In a healthy eye, the rate of secretion balances the rate of drainage [12]. In Glaucoma candidates, the drainage canal is partially or completely blocked. Fluid builds up in the chambers and causes an

increase of pressure within the eye [13]. The pressure drives the lens back and presses on the vitreous body, which in turn compresses and damages the blood vessels and nerve fibers running at the back of the eye. These damaged nerve fibers result in patches of vision loss, and if left untreated, may lead to total blindness [14].

There are two common types of Glaucoma: Open Angle and Angle Closure Glaucoma [15]. Open Angle Glaucoma is caused by a partial blockage of the drainage canal, where the angle between the cornea and the Iris remains open, but the flow of aqueous humor is very slow [16]. The pressure builds up, gradually, in the eye over a long period of time. Symptoms also appear gradually, starting from simple vision loss, and may go unnoticed until the central vision is affected. The progression of Glaucoma can be prevented with medical treatments, but part of the vision that is already lost cannot be restored [17]. This is why it is very important to detect early signs of IOP leading to Glaucoma with regular eye exams like Tonometry test, Ophthalmoscopy test, Perimetry test, Gonoscopy test, and Pachymetry test [18, 19]. On the other hand, Angle Closure Glaucoma is a medical emergency and requires immediate attention. It is caused by a sudden and complete blockage of aqueous humor drainage [20, 21]. Here, the pressure within the eye rapidly rises, and the result may lead to a quick vision loss. Certain anatomical features will be presented inside the eye such as narrow drainage angle, shallow anterior chamber, and a thin and droopy Iris.

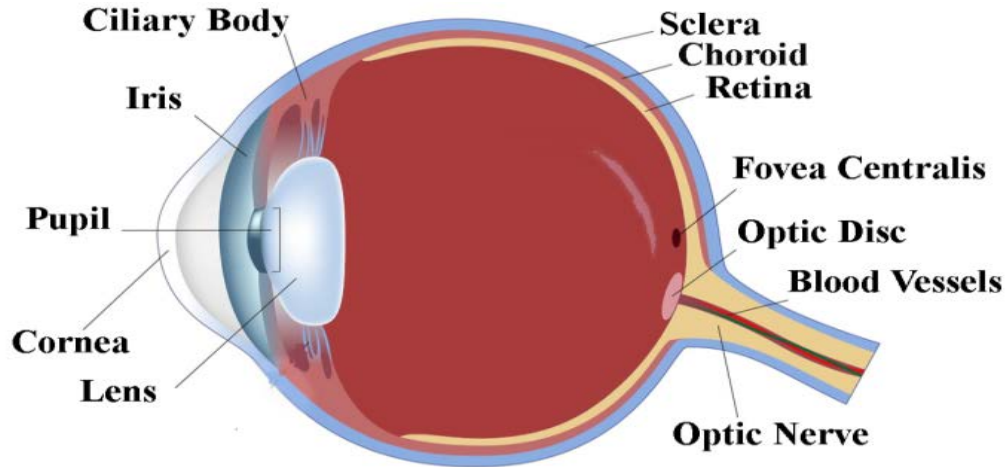


Figure1.1 General Depiction of the human eye.

Aside from abnormal eye liquid build-up, in many Glaucoma candidates, other factors contribute to the onset of the Glaucoma condition through medication unrelated to eye disease. Many drugs taken by patients for anxiety or depression affect the brain, and physiological composition of the body [22]. This includes the muscles in the eye that control the Pupil size.

This study introduces an image processing technique from frontal eye images to monitor and help in the initial diagnosis of potential rise of IOP. It extracts certain features from the contour of the sclera and measures the redness level and red area percentage of the sclera. The work also calculates the ratio of the Pupil and the Iris diameter, as one of the discriminating features of IOP.

1.3 Contributions of the Proposed Research

In this study, the development of an intraocular pressure detection simulation framework that aids patients with potential high eye pressure in their monthly clinic visits

is proposed by enabling doctors/individuals to initially monitor the patients' eye pressure by non-contact means, non-invasively.

The novelties and contributions of this dissertation from a theoretical point of view include: introducing a fully convolutional network architecture for eye sclera segmentation, in addition to scientifically correlating the frontal eye view (image) with IOP by introducing new sclera contour features that have not been previously introduced in the literature from frontal eye images for IOP status determination. Glaucoma and IOP determination from the frontal eye view has only been experimentally practiced in Traditional Chinese Medicine and Acupuncture [23, 24].

This work shows that there is evidence of computational relationship between the IOP status and frontal eye image features. From the applicative view-point, this work is contributing to the development of an initial monitoring framework determining the status of IOP from only frontal eye images.

In computer vision, the image goes through a cascade process until the final target is achieved. Pre-processing techniques are applied to the frontal eye images in order to start the actual process of extracting the features. These include a red layer that is obtained to remove the noise, and then a canny edge detection technique [25] that is applied to reduce the amount of data in the image. After that, the system enhances the edges by applying the gamma adjustment and automated thresholding technique [26]. After pre-processing techniques have been applied, two experiments have been adopted in this study to extract the features. In the first experiment, five features have been

extracted from the frontal eye images: Pupil/Iris ratio, RAP, MRL, contour height and contour area. The sclera has been extracted using the Circular Hough Transform (CHT) technique and the RAP, MRL and sclera contour features have been calculated from the whole sclera. After extracting the features, classification techniques have been applied in order to detect the status of IOP; either normal (healthy) or high IOP (un-healthy). In the second experiment, six features have been extracted from the frontal eye images: Pupil/Iris ratio, RAP, MRL, contour distance, contour area, and contour angle. The sclera itself has been extracted using a fully convolutional network (FCN) technique in the second experiment. The RAP and MRL features have been extracted from a rectangular region of interest from the segmented sclera. The sclera contour features have been extracted from a triangular region of interest from the segmented sclera. After extracting the six features, classification techniques have been applied in order to detect the status of IOP. SVM and DT were applied in order to train and test the images and obtain a risk assessment result for intraocular pressure.

CHAPTER 2: LITERATURE REVIEW

Many researchers have proposed several works on the issue of IOP detection and analysis of the eye from images. However, there is a lack of studies regarding IOP based on frontal eye images in the computer vision field. Most of the studies focus on fundus images that show the status of the optic nerve or investigate relevant feature extraction for purposes other than IOP. Moreover, some studies require additional hardware/devices with direct contact to the eye to measure IOP.

Mariakakis et al. [27] proposed an approach to assess intraocular pressure using a smartphone and a hardware adapter attached to it. The adapter is a clear acrylic cylinder that is connected to the camera of the smartphone, with a diameter of 8mm and height of 63mm. The authors stated that only trained users must use this device. The user holds the smartphone perpendicularly over the patient's eye and then applies the weight of acrylic cylinder to it. The smartphone camera would then start recording the appplanation of the eye. Video analysis is then applied to measure two ellipses, the acrylic cylinder (outer ellipse) and the appplanation surface (inner ellipse). The ellipses are then mapped to absolute measurements of the diameter of the acrylic cylinder. The final diameter measurement is mapped to an IOP value using a clinically validated table such as the one published by Adolph Posner [28]. As stated by the authors, this device cannot be deployed by ordinary users and the patient must visit the clinic.

Gisler et al. [29] proposed a glaucoma detection technique using intraocular pressure monitoring. The data was supervised by Sensimed Company where contact lens sensors (CLS) were used to automate recording the continuous ocular dimensional changes over 24 hours. The CLS system is safe and non-invasive. However, a health care professional is required to install it and remove it from the patient. The authors used Java software to manage the data and feature extraction. The feature extraction was split into two parts. The first part included statistical features (raw frequency values and filter banks) and the second part consisted of physiological features (eye blinks, ocular pulse and slope of the curve), which were fed to a support vector machine (SVM) classifier [30].

Shahiri et al. [31] proposed a micro electromechanical pressure sensor for measuring IOP based on P++silicon. Finite element analysis (FEA) was used to simulate, optimize and analyze the mechanical properties of the device. The authors investigated the deformation in the Z axis of the diaphragm with a thickness of 4mm at applied pressure of 30 mmHg. The authors found that the deflection of the center of the diaphragm varies linearly with the range of pressure.

The work in [32, 33] used fundus images to identify the visual field defect and detect Glaucomatous progression. The authors used the Gaussian Mixture Model (GMM) clustering method based on inspection points of the fundus images to incorporate the distance between these points.

Table 2.1 Summary of related techniques.

Algorithm	Ref.	Characteristics and performance.	Data type
Smartphone-based system for assessing intraocular pressure	[27]	<ul style="list-style-type: none"> • Measuring the eye pressure. • Smartphone used. • Patient must buy an adapter connected to camera. • Technique must be operated by a specialist (not the patient). • Video recording by smartphone camera. • Physical contact with eye in order to apply pressure on the cylinder. • Accuracy: N/A. 	<ul style="list-style-type: none"> • Video frame images
Glaucoma detection using intraocular pressure monitoring	[29]	<ul style="list-style-type: none"> • Monitoring IOP. • Use of special contact lenses with sensor. • Java software used to manage data and for simulation. • Specialist must help in order to install and remove the contact lenses sensor. • Accuracy : N/A. 	<ul style="list-style-type: none"> • Contact lens sensor
Micro-electromechanical pressure sensor for measuring intraocular pressure	[31]	<ul style="list-style-type: none"> • Measuring IOP based on P++silicon. • Finite element analysis (FEA) used for simulation. • Pressure applied on the eye. • Accuracy: N/A. 	<ul style="list-style-type: none"> • Pressure sensor
Glaucoma Detection Progression	[32, 33]	<ul style="list-style-type: none"> • Visual field defect. • Glaucomatous progression. • Fundus images used. • Mixture of Gaussian and Generalized Expectation Maximization (GEM) techniques. • Specificity : 96% ; Sensitivity : 87% ; Accuracy : N/A. 	<ul style="list-style-type: none"> • Fundus Images

<p>Proposed IOP Risk Assessment</p>	<ul style="list-style-type: none"> • Segment the Iris and Pupil with accuracy of 95.30%. • Extract the sclera. • Measure the Mean Redness Level with accuracy of 96.06%. • Measure the Red Area Percentage with accuracy of 98.80%. • Segment the sclera, measure area and height or distance and angle features of the extracted sclera contour. • Frontal images used. • No need for specialist to take the image. • Controlled environment (closed room with lights on). • SVM, DT and Neural network tested • Over 96.0% Test Phase Accuracy. 	<ul style="list-style-type: none"> • Regular camera images
--	---	---

Table 2.1 provides a comparison of our IOP risk assessment estimation framework with other related techniques. It is important to mention that however, no prior related work used frontal eye images for IOP risk determination. Therefore, the table only provides a summary of the related techniques, the image database and performance and/or application. A summarized comparison of the approaches/devices that used different inputs/sensors (e.g. fundus images) for a similar purpose or output like IOP, is provided in the table.

2.1 Related Work on Blood Vessels Detection

Bendaoudi et al. [34] proposed retinal blood vessels detection architecture using match filter and Gaussian algorithms applied on high resolution fundus images for diabetic retinopathy patients. Almi'ani, and Barkana [35] presented an image segmentation algorithm that was applied on Magnetic Resonance Angiography (MRA)

images by using a matched filter technique to segment the vascular structure of brain based on a region growing method. Hassan and Azis [36] applied opening reconstruction and Top-Hat transform techniques on fundus images for blood vessels segmentation and extraction. Researchers in [37] proposed a low complexity process for vessels segmentation applied to fundus images for the Drive database [38] by combining two morphological operators in two channels, the Green and L channels. Authors in [39] displayed a process of blood vessels segmentation applied to State and Drive databases [40]. This process began with the selection of the green channel of the fundus image, that was, then, subtracted from the obtained background image and the smoothed image was applied. As a result, the image was normalized and stretched by calculating the mean of local histogram. Finally, a global threshold was applied to segment the vessels.

Nikhil et al. [41] presented a mechanized picture handling framework that distinguishes the anomaly as Proliferative Diabetic Retinopathy (PDR) by using an image subtraction system and Severe Diabetic Retinopathy (SDR) utilizing the thickness of the eye's liquid location procedure. Luo et al. [42] proposed a method to detect and measure the vessels by the Gaussian function and an amplitude-modified second order Gaussian filter. The authors claim that their scientific dissection is given and backed by reproduction and trials to show that the vessel width might be measured in straight association with the "spreading factor" of the matched filter when the extent coefficient of the filter is suitably allotted. Maria et al. [43] displayed a mechanized system for the division of the vascular system in retinal pictures. The calculation begins with the extraction of vessel centerlines, which are utilized as rules for the ensuing vessel filling

stage. Four directional differential operators are handled with a specific end goal to choose associated sets of potential focuses to be further classified as centerline pixels utilizing vessel-determined methods. The final division is acquired utilizing an iterative area developing system that incorporates the substance of a few paired pictures coming about, because of the vessel width subordinate morphological filter. Oakar et al. [44] displayed the scientific morphology strategy to identify the optic circle (OC) and the veins. The location of optic plate and the veins are the important steps in the identification of diabetic retinopathy; in light of the fact, that the veins and the optic circle are the typical features of the retinal picture. Furthermore, the optic circle and the exudates are the brightest part of the picture. Identification of the optic plate and the veins can help ophthalmologists catch infections earlier and much quicker. The optic plate and the veins are distinguished by utilizing numerical morphology strategies, for example, shutting, filling, and morphological remaking. Correct estimation of vessel distances across the retinal pictures has a critical impact in diagnosing cardiovascular maladies and early indications of certain systemic infections: such as diabetes and hypertension. Nidhal et al. [45] created a new technique to focus on the width of retinal veins by investigating the shade fundus picture. Retinal vessel breadth was measured around the vein divider when evaluating the advanced fundus picture. Moreover, [45] proposed a reliable and precise method to determine the measurement (width) of a retinal vein around a recommended vein specifically chosen to measure across the vein distances. The calculations were done by uprooting the bifurcations and focusing on the width for each vein fragment. Soju et al. [46] examined images to concentrate on distinctive peculiarities. As exudates, microaneurysms, and anomalous development of veins are a

percentage of the manifestations of DR, preprocessing of the image is constantly needed to acquire a picture of the improved complexity. The authors in [46] gave an outline of a percentage of the preprocessing procedures utilized until now, and diverse strategies to concentrate exudates, microaneurysms, and veins.

Robotized picture transforming methods can support the early discovery of diabetic retinopathy ailments, which could be viewed as an indication of diabetes on the retina. Vein division is the fundamental component for creating retinal screening frameworks, since vessels serve as one of the principal retinal milestone characteristics. Osareh et al. [47] proposed a mechanized strategy for detecting veins in shade pictures of the retina. For each picture pixel, a certain vector that uses properties of scale and specific Gabor channels is processed. The concentrated vectors are then arranged utilizing the generative Gaussian mixture model and discriminative support vector machine classifiers.

Computerized pictures are acquired from the retina and reviewed by experts. Movement of diabetic retinopathy is evaluated by its seriousness, which decides the recurrence of examinations. In any case, machine-helped observations have been developed to address an essential inadequacy of those master spectators. Evaluation of the vein framework plays an essential part in a variety of therapeutic issues. Signs of a few vascular issues, diabetic retinopathy for example, rely on identification of the vein system. Yashowardhan et al. [48] introduced another administered strategy for vein location in computerized retinal pictures. The authors proposed depicting vascular retinal picture division and extraction of system calculations, known as multi-scale single-

channel linear tracking (MSLTA). The obtained pictures give an interesting view of the eye vasculature. The examination of the vasculature is highly critical, particularly for locating cardiovascular infections. Moreover, the authors presented a multiscale calculation method for programmed retinal vein division, which is considered a prerequisite for the judgment of vascular ailments. This calculation started by selecting a seed pixel in the picture, and then selecting subsequent pixels that meet the criteria so long they provide a higher trust level.

Jaspreet et al. [49] created a programmed framework for the extraction of typical and unusual peculiarities in shade retinal pictures by using a filter-based approach with a bank of Gabor filters to segment the vessels. The recurrence and introduction of a Gabor channel are tuned to match that of a piece of vessel to be concentrated in a green channel picture.

Safia et al. [50] did a comparison between two different methods. The first procedure utilized Gaussian sifting for preprocessing, Log separating for improvement, and versatile thresholding for division reasoning. The second procedure utilized unsharp concealing for preprocessing, the Gabor wavelet for improvement, and worldwide thresholding for division.

Reyhaneh et al. [51] introduced another technique for discovering vessels in retinograms. The Dual-tree Complex Wavelet Transform (DT-CWT) was utilized to give a rich, multi-scale depiction of nearby structures, and an arbitrary Woodland-based classifier was utilized to group pixels as vessel/non-vessel on the premise of their DT-

CWT coefficients. Lassada et al. [52] proposed a consequence of a correlation of edge location strategy for programmed characterization of retinal veins in newborn child pictures. The correctness of each technique is analyzed by contrasting the results and hand-drawn ground-truth pictures.

Joes et al. [53] introduced a system for robotized division of vessels in two-dimensional color pictures of the retina. This system might be utilized within a mechanized screening for diabetic retinopathy. The framework was focused around extraction of picture edges, which match more or less with vessel centerlines. The edges were utilized to make preliminary images as line components. With the line components, a picture was apportioned into patches by doling out each pixel to the closest line component. Each line component constituted a nearby arrangement outline for its related patch. For each pixel, characteristic vectors were calculated making use of properties of the patches and line components. The peculiarity vectors were arranged utilizing the kNN classifier and a successive forward method choice.

2.2 Related Work on Pupil/Iris Detection

Patange and Jagadale [54] presented an image processing framework using slit lamp frontal images to improve detection and gradation of cataract disease by inserting the image in a cascade process. This process included image acquisition, Pupil extraction, feature extraction, cataract detection and gradation. Hung and Zhang. [55] proposed a method to study the effect of physical exercise on Pupil Size Variability (PSV) spectrum. The authors detected the Pupil using canny edge detection, unrelated edge removal and

ellipse. The area of the resulting ellipse fit the Pupil size. The study showed that the Pupil size contained a huge amount of physiological and physical information equivalent to the heart rate (HR) and blood pressure variability (BPV). Authors in [56] displayed a mechanized system to observe the changes in the Pupil size under the influence of circular objects that have different sizes and levels of brightness generated from an LCD screen in order to stimulate the central point of the retina. The authors detected the Pupil by applying simple thresholding technique and blob analysis. In addition, they used a full horizontal scanning of the image to detect the boundaries of the Pupil. Once the author detected the boundary points of the Pupil, they utilized an elliptical shape to measure the area of the Pupil.

Du et al. [57] presented a video-based Iris segmentation method for non-cooperative situations. The authors used the k-means clustering algorithm to estimate the valid specular reflection and to detect the cluster. Principle component analysis (PCA) was also used to reduce the dimension of clustering centers. Finally, a direct least square fitting of ellipse was used to fit the Iris and Pupil.

2.3 Optic Nerve based on Fundus Images

Yousefi et al. [32] worked on fundus images to demonstrate a pipeline to cluster the visual field into two categories, the normal and the Glaucoma. The Glaucoma category was clustered into two patterns, the stable and the progression. The authors modeled the visual field data using the mixture of Gaussians approach and the Generalized Expectation Maximization (GEM) technique. Each cluster was decomposed

into several axes using Principal Component Analysis (PCA) to recognize any Glaucomatous progression. Yousefi et al. in [33] also provided a method for Glaucoma progression detection using Machine Learning Classifiers (MLC's) from fundus images. The optic disc images and the thickness of the surrounding retinal nerve fiber layer were taken by using the Optical Coherence Tomography (OCT). A combination of several classifiers such as Bayesian, Instance-based, Meta, and tree families of MLC's plus Bayesian net were used.

2.4 Redness of the Sclera

Cullen et al. [58] measured the redness in the sclera from frontal eye images caused by the contact lenses. The authors started computing the level of redness by extracting the sclera, and then, canny edge detection was applied to measure the total length of the vessels. Finally, the authors determined the redness level by computing the sum of the redness of each pixel.

2.5 Related Work on Mechanisms of Elevated Intraocular Pressure

Morphologic adjustments in the extracellular network of the fluid surge framework in patients with glaucoma have been depicted in subtle element [59-61]. Quickly, these progressions incorporate nodular expansion of extracellular collagen, discontinuity, and "twisting" of the collagen fiber groups. There is an incremental increase in glycosaminoglycan content [59] with a general lessening in hyaluronic corrosive [62]. The endothelial cells lining the trabecular meshwork show "frothy" degeneration with cellar layer thickening [63]. Ultrastructural changes in the

juxatacanalicular tissue—the furthest part of the trabecular lattice work accepted to be the in all probability site of obstacle in glaucoma—have additionally been portrayed [59, 64, 65]. There is gathering of nonfibrillar material with attributes of stroma cellular film, wavy collagen, and chondroitin sulfate protein complex. Changes in grid vesicles (extracellular lysosomes), sheath material from subendothelial flexible like strands, extracellular glycoprotein, fibronectin, and elastin have been accounted for in [64, 66]. The specificity of a portion of the morphologic changes has been addressed on the grounds that comparative discoveries have been noted in ordinary matured eyes without glaucoma [67]. This has driven some to theorize that glaucomatous changes in the outpouring pathway may speak to a quickened maturing process [68]. Notwithstanding the adjustments in the trabecular meshwork, the breakdown of Schlemm's channel has been conjured as another system of surge block [69]. To bolster this theory, attachments between the internal and external dividers of Schlemm's channel have been indicated [59-69].

2.6 Related Work on Optic Disc and Visual Field Changes

Typical optic plates show sound wave in place of neural edges, while conditions that can be confused for glaucoma incorporate compressive or infiltrative sores of the optic nerve, past ischemic optic neuropathy (arteritic and non-arteritic), inborn and genetic optic neuropathies, post-traumatic optic neuropathy, provocative and demyelinating optic neuritis. Most cases in the compressive classification of intracranial mass sores that cause optic nerve or chiasmal pressure will be pituitary adenomas, craniopharyngiomas, suprasellar aneurysms, or meningiomas. Numerous causes, such as,

tumors will exhibit in patients who are more youthful than the normal glaucoma persistent cases [70, 71].

Patients with compressive harm may display visual fields that look like those of glaucoma tolerant, with arcuate or nerve fiber group misfortune and shallow optic circle measuring. On the other hand, it is optic nerve whiteness in overabundance of measuring, especially of the worldly edge that ought to provoke the doctor to look for etiologies other than glaucoma. A vertical stride in the visual field, from inclusion of the intersection of the optic nerve and chiasm or the chiasm itself, ought to likewise alarm the clinician of conceivable pressure or penetration, as opposed to a cecentral scotoma or diminished keenness [67, 72].

Ischemic optic neuropathy may result in nerve fiber bundle field loss if seen after the disc swelling is resolved. Arteritic ischemic optic neuropathy may bring about measurement similar to glaucoma, from a loss of plate substance delivered by significant ischemia. Nevertheless, this is typically joined by checked central blood vessel narrowing close to the disc, and the patient may give a historical documentation regarding loss of sight with a cause of headache, jaw claudication, weight reduction, anorexia, or fever. In non-arteritic ischemic optic neuropathy, the contralateral disc may have a small cup; the included eye may have altitudinal paleness without cupping but with retinal blood vessel narrowing.

The third class, innate and inherited optic neuropathies, comprises of conditions that can bring about optic nerve appearance and visual field misfortune that likewise look

like glaucoma. Cases of such sicknesses incorporate autosomal predominant optic decay, papillorenal disorder, optic nerve head pits and colobomas, prevalent segmental optic nerve hypoplasia and Leber's genetic optic neuropathy. A cautious history and the span and/or movement of the clinical discoveries are useful and enlightens to set the right determinants [71, 72, 73].

Other uncommon reasons for pseudoglaucomatous optic nerve alteration incorporate late changes after methanol-lethality and late changes in tertiary syphilis. The history is normally useful in harmful optic neuropathy, yet identification (ID) of syphilis may oblige lab testing [74, 75].

2.7 Related Work on Mechanism of Optic Nerve Damage

Verifiably, glaucomatous optic nerve harm has been ascribed to either a mechanical or vascular etiology. It is improbable in any case that, either hypothesis alone will completely clarify the optic nerve harm in glaucoma. Primary open-angle glaucoma (POAG) has been extensively described and studied through major research studies, including elevated intraocular pressure, advancing age, family history, African ancestry, myopia, and perhaps presence of certain systemic diseases, such as diabetes and hypertension. The precise mechanism of increased resistance to aqueous outflow remains unclear and is currently an active focus of research [76].

2.8 Related Work on Mechanical Considerations

Both in vitro and in vivo studies have demonstrated that raised IOP can bring about back bowing of the lamina cribrosa, the collagenous structure that backs the retinal

ganglion cell axons as they leave the eye [70, 77]. The lamina cribrosa is comprised of about 10 parallel plates, each with different measured pores that permit packs of axons to go through but then keep up the capability of the eye to hold weight. Confirmation recommends that the plates of the lamina cribrosa are packed in POAG and may completely give way now and again [78]. Such physical twisting of the lamina cribrosa is thought to harm the passing axons, either by contortion or crimping. Different studies have indicated prolongation of the pores inside of the lamina cribrosa, recommending mechanical strengths that may extend and section the littler shafts [79]. Changes in the extracellular network have been portrayed and that may prompt the loss of auxiliary backing in the lamina cribrosa [80-82]. These progressions incorporate cellar layer thickening, complicated and divided laminar bars, expanded level of specific sorts of collagen, and basic changes in elastin. Elucidation of these morphologic changes inside of the lamina cribrosa ought to be done circumspectly; on the grounds that they may speak to optional as opposed to essential changes in glaucoma [82].

There is confirmation that the increase of IOP can obstruct axoplasmic; also known as axonal transport, a cellular process responsible for movements of mitochondria, lipids, synaptic vesicles, proteins, and other cell parts (i.e. organelles) to and from a neuron's cell body through the cytoplasm of its axon; stream inside of the retinal ganglion cell axon. Axonal transport is key to the typical working of neurons; retrograde axonal transport of target-determined neurotrophic components may be vital for cell survival. It has been proposed that increased IOP may prompt the degeneration of retinal ganglion

cells, by meddling with retrograde exoplasmic stream of fundamental neurotrophic components [79, 80].

2.9 Related Work on Vascular Considerations

Defenders of the vascular hypothesis contend that microvascular changes in the optic nerve head are in charge of glaucomatous optic nerve harm [70, 83]. Blood supply to the prelaminar and laminar ranges of the optic nerve is obtained from the peripapillary choroid and short back ciliary conduits. The vascular supply to the foremost optic nerve may be bargained in glaucoma through a few distinct systems [84]:

- 1) The capillary network of the optic nerve head may be selectively lost in POAG. Another study however, showed that the retinal ganglion cell axons and the capillary network are lost at the same rate, suggesting that there is no selective loss or pre-existing damage to the capillary network.
- 2) Hayreh noted the importance of the “watershed” zones of the choroidal blood supply. The watershed zones refer to the border areas between various choroidal segments, each supplied by a short posterior ciliary artery. The watershed zones represent potential areas of compromised circulation and can include the optic nerve head. In addition, nocturnal systemic hypotension has been proposed as an additional risk factor for the development of glaucoma.
- 3) An epidemiologic association between POAG and systemic microvascular disease (*e.g.*, diabetes mellitus) has been reported. Other studies have failed to show a significant correlation between POAG and diabetes. However, there is some

evidence that autoregulation of blood flow in the optic nerve head is altered in POAG. Autoregulation is an important mechanism by which arterioles dilate or constrict with the rise or fall in perfusion pressure to maintain constant blood flow to the retina. In glaucoma, this auto regulatory mechanism may be defective and may predispose the optic nerve to ischemic damage.

CHAPTER 3: RESEARCH PLAN

In this study, we developed an IOP estimation simulation framework based on the Pupil/Iris diameter ratio, the mean redness level (MRL), the red area percentage (RAP), and features of the sclera contour from frontal eye images. Our final results of the grade level of IOP are recorded in percentages using machine learning classifiers. Figure 3.1 shows an overall view of our framework. The simulation is carried out by MATLAB 2014a software.

3.1 Material (Database of Images)

In this study, we used the image database¹ (DB) from Princess Basma Hospital (Jordan-Irbid) which was generated in 2014 and completed in 2016. Four hundred participants contributed to the database of images. Half of them were patients with high eye pressure. The other half of the participants represented normal eye pressure cases. The age ranges of the patients were between 40 and 65 years old (which generally represent the age range of high IOP cases). Each patient's level of eye pressure was recorded in the database by ophthalmologists and the images were labeled as high or

¹ IRB approval has been obtained at Princess Basma Hospital for the human subject samples. We formally requested access to the dataset.

normal IOP. The IOP range of the 200 normal eye pressure cases were 11-20 mmHg (with mean of 14.7 mmHg) and the range of the 200 high eye pressure cases were 21-30 mmHg (with mean of 24.7 mmHg). The IOP cutoff used in this research is 20 mmHg as advised by the ophthalmologists. If the participant has $IOP \leq 20$ mmHg, it is normal, otherwise it is considered as high IOP. All the database images were taken in a range of 20 cm between the camera and the patients. All eye images were taken in the same lighting conditions. The normal and high IOP images were stored in two different folders. Each image was saved in JPG format. The camera used was a canon camera model T6-K1 with resolution 3241×2545. This resolution can be found in any smartphone nowadays.

3.2 Method

In this research, we developed a smart computer vision-based IOP risk estimation framework based on features extracted from the frontal eye images. Two experiments have been adopted to detect the status of the eye. Each eye image first goes through a preprocessing stage to prepare the images for feature extraction. The features are Pupil/Iris ratio, mean redness level (MRL), red area percentage (RAP) and sclera contour features (area, height or distance, angle). Our final result of the grade level of IOP risk is displayed as eye status: normal or high IOP. The final results come from scaled values computed using a neural network (NN). Support Vector Machine (SVM) and Decision Tree (DT) machine learning classifiers are also applied in the experiments. Figure 3.1 shows an overall view of our framework. The development is carried out by MATLAB 2014a software.

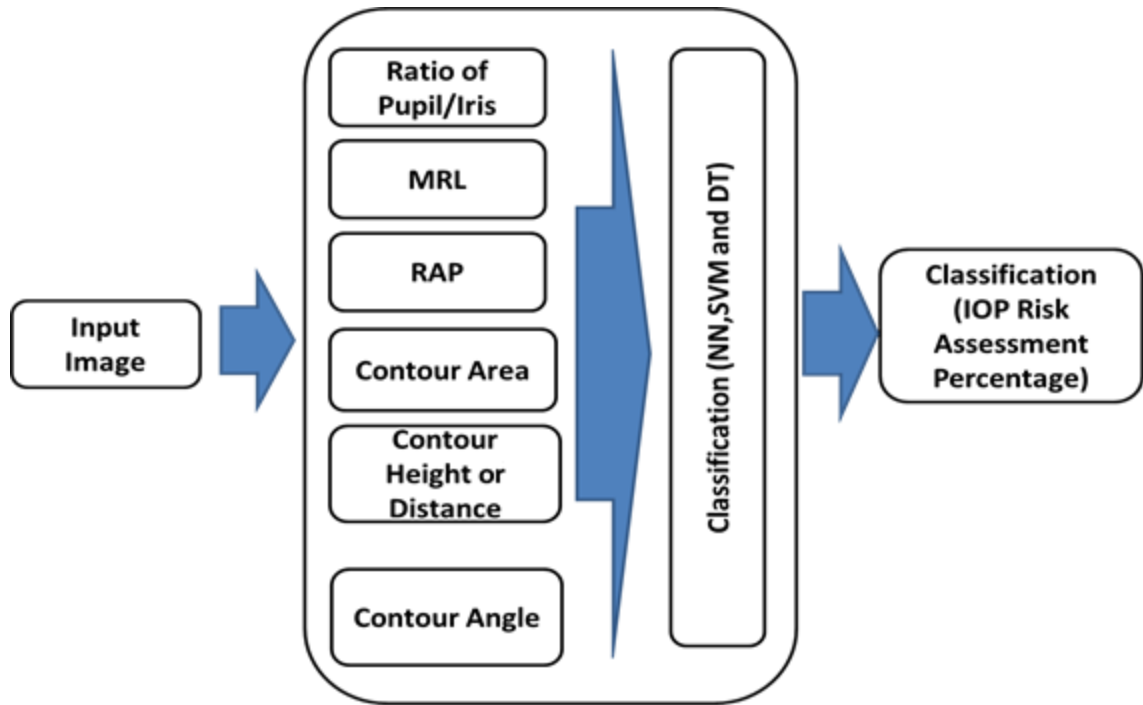


Figure 3.1 IOP risk assessment framework. First experiment features: Pupil/Iris Ratio, MRL, RAP, Contour (Area, Height). Second Experiment: Pupil/Iris Ratio, MRL, RAP, Contour (Area, Distance and Angle).
 First experiment Classifiers: SVM, NN. Second Experiment Classifiers: SVM and DT.

3.3 Pre-Processing

Prior to feature extraction, the Adaboost face detection algorithm and haar cascade eye detection [85, 86] (as shown in Figure 3.2) are applied to the face images in order to extract the eye image automatically. Each eye area segment was extracted as a rectangle.

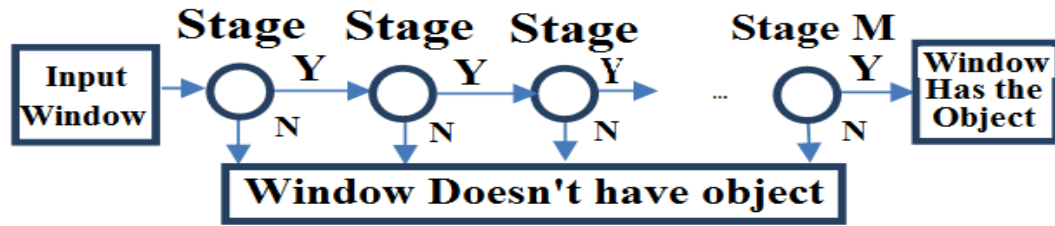


Figure 3.2 Haar cascade classifier to detect object.

After extracting the eye image, different steps at the preprocessing stage are applied in order to extract the Pupil, Iris and sclera, as shown in Figure 3.3.

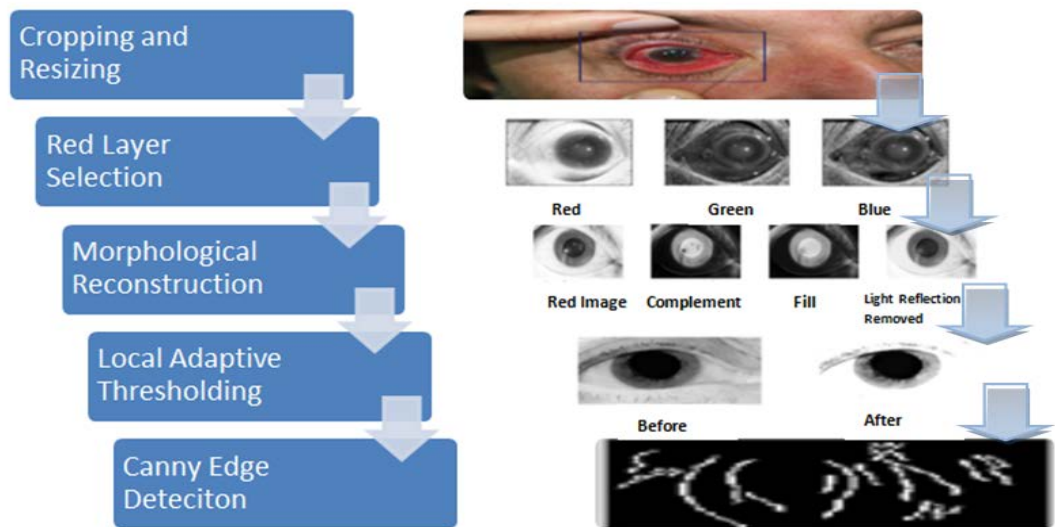


Figure 3.3 Pre-processing stage to extract Iris and Pupil.

In the first step, the image is cropped and resized to set the Height:Width ratio to be 1:1.8, respectively. Then, the red layer $I(:, :, 1)$ image is extracted because it discards unwanted data and enhances the Iris and the Pupil area (we use the red layer here just to detect the Pupil and the Iris). After that, a morphological reconstruction technique [87] is

applied on the red layer image in order to remove the light reflection (which is often seen as a bright circle) on the Pupil. Removing the light reflection here is considered as an important step since we will use the Circular Hough Transform (CHT) technique [88] to detect the Pupil and Iris. Then, local adaptive thresholding [89] is applied to separate the foreground from the background. Canny edge detection [90], which is considered as one of the most well-known techniques to detect edges, is then applied to detect the edges of the eye image. Canny edge detection consists of three main techniques: Gaussian filter [91], Non max suppressions (NonMaxSup) [92] and Hysteresis thresholding (Hysthresh) [93]. After applying several experiments using the canny edge detection function, it has been observed that the best values for the parameters to generate edge images are the ones shown in Table 3.1.

Table 3.1 Typical parameter values of canny edge, gamma, radius and thresholding

	Iris	Edge Image	Pupil Edge Image	Eyelids Edge Image
Sigma		1	1	1
VERT		0.7	0.7	0.2
HORZ		0.3	0.3	0.8
Gamma		1.3	1.4	2
Radius		1.35	1.5	1.35
T1		0.1	0.1	0.1
T2		0.099	0.099	0.099

The gamma values for canny edge detection are also shown in Table 3.1. The gamma value is part of the adjust Gamma “adjgamma” function [94] that changes the contrast of an image. After applying canny edge detection, a Circular Hough Transform (CHT) technique applied in order to extract the Iris and Pupil, as shown in Figure 3.4.

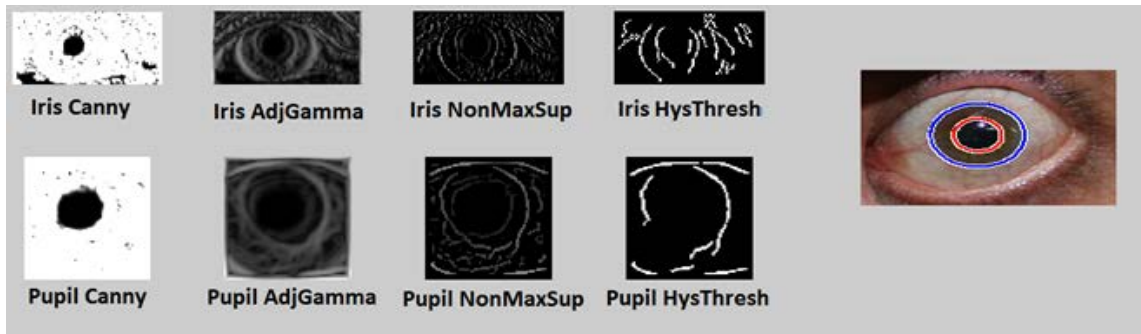


Figure 3.4 Iris and Pupil detection using CHT technique.

3.4 First Experiment (Sclera segmentation using CHT)

The CHT function has one disadvantage. It performs poorly when a large part of the circle to be detected is outside the image. This is not a problem for detecting the Pupil or Iris circles since both of them are found completely in the image. However, for detecting the upper and lower eyelid circles, this issue would come into picture. To work around this problem, we extend the images by a black area either from the top (when detecting the lower eyelid) or from the bottom (when detecting the upper eyelid), as shown in Figure 3.5.



Figure 3.5 Extended eye image.

Moreover, the only circle that is detected without cropping or deletion is the Iris circle, after which we use the Iris circle parameters to modify edge images and ease the job of finding other circles. For example, before detecting the Pupil, the edge image will be cropped to a square with center equal to the Iris circle center and sides just less than the Iris radius. This makes the detection of the Pupil circle much easier as we do not need all the details outside the Iris.

Now the Pupil Radius/Iris Radius ratio can directly be calculated and ready to be used. Sample results are shown in Figure 3.6. The blue circle is for the Iris, the red for the Pupil, the yellow for the upper eyelid and green for the lower eyelid.

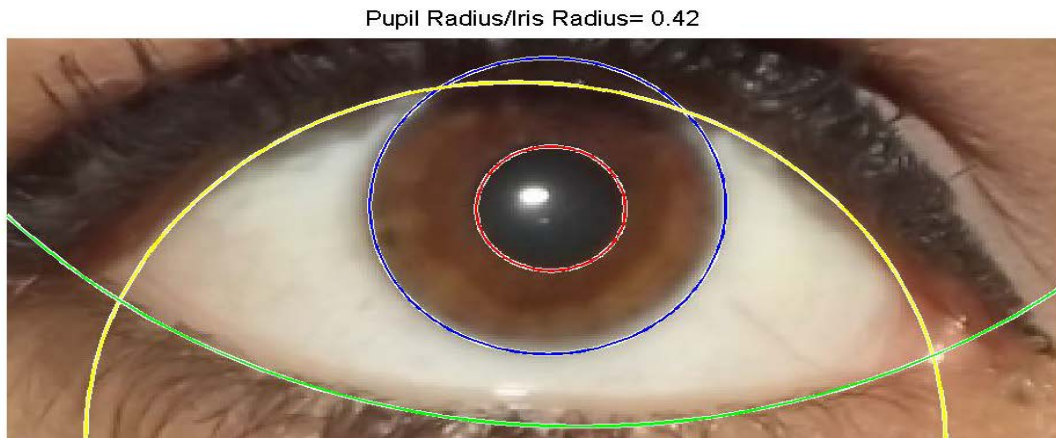


Figure 3.6 Detecting Pupil/Iris and eyelids.

After detecting the circles (Iris, upper and lower eyelids), segmenting the sclera becomes more clear. The sclera would be the area included between the intersection of the upper and the lower eyelid circles except for the Iris circle. So, for a pixel to be in the

sclera region, it should be inside both the upper and lower eyelid circles but not in the Iris circle. Knowing the equation of a circle is:

$$(x - a)^2 + (y - b)^2 = r^2 \quad (3.1)$$

where (a, b) is the center coordinates and r is the radius, and since any horizontal line passing by the circle $y=\text{constant}$ will cut the circle into two areas, the locus of all points of that horizontal line that are inside the circle will be:

$$a - \sqrt{r^2 - (b - y)^2} \leq x \leq \sqrt{r^2 - (y - b)^2} + a \quad (3.2)$$

$$\text{where } b - r \leq y \leq b + r$$

In the Equation, variable x is replaced by “col” and y is replaced by “row”, so we can use the above simple formula to get all pixels inside a circle in the image. This way, we were able to extract the sclera, as shown in Figure 3.7 (the sclera image is denoted as S).



Figure 3.7 Extracted sclera.

3.5 Second Experiment (Sclera segmentation using FCN)

Sclera segmentation is a challenging process especially that in cases of high IOP, Cataract and Glaucoma, most of the sclera area becomes red. For that reason, a robust segmentation algorithm is required that can handle such cases. In the last couple of years, deep learning with convolutional neural network (CNN) has shown promising results in semantic segmentation for objects [95-99]. Most of these network structures are complicated and time consuming, especially to be implemented on smart-phone devices. In this dissertation, a modified version of the fully convolution network (FCN) structure in [95] is introduced for its simplifications over other structures. The proposed FCN consists of convolutional layers for feature extraction without any fully connected layers. At the later stages of the network, deconvolutional layers are used to resize the image back to its original size. The network structure of the proposed network is represented in Figure 3.8. To improve segmentation edges, the last stage results are added to early stages to use the edge features generated in the early stages. As shown in the Figure, each convolution stage includes a Rectified Linear Unit (ReLU) activation function, and at the end of each stage, maximum pooling is used to down sample the extracted images. Chapter 5 will include a sample of the results for this trained network versus applying Hough transform for sclera segmentation.

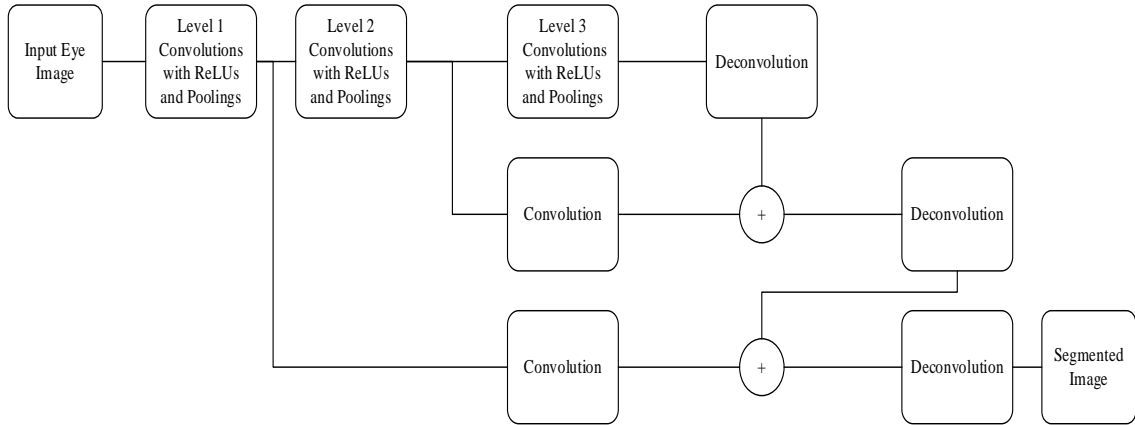


Figure 3.8 Fully Convolutional Network (FCN) structure for sclera segmentation.

The segmentation technique is implemented using the Caffe toolbox with Python wrapper on an Nvidia Titan x GPU. Since the sclera segmentation process should work with any frontal eye image (with or without eye diseases), the collected dataset images along with other normal frontal eye images collected over the internet (such as the images from the publicly available databases used in [100]) are combined (normal and high IOP) and grouped into two groups, training and testing groups. To increase the number of images in the dataset, data augmentation techniques have been used by 2D transformations of the eye images. The total number of images achieved for this segmentation process is 858 images from different people of various races. Half of these images are used for training and the other 50% are used for testing. The weights of the designed network are initialized by transfer learning from the segmentation network designed in [95]. Softmax loss function is used and solved with the Stochastic Gradient Decent optimization (SGD) technique. Results of the proposed network for segmentation can be found Table 3.2. Mean accuracy, pixel accuracy (overall accuracy) and region intersection of union (IU) are used as metric results for the segmentation process.

Formulations for these metrics are presented in Equations 3.3-3.5. Examples for the FCN segmentation results are shown in Figure 3.9. As can be seen from the Figure, the proposed FCN network shows improved segmentation performance over Hough transform, as used in [101, 102].

$$\text{Pixel Accuracy} = \frac{\sum_i n_{ii}}{\sum_i t_i} \quad (3.3)$$

$$\text{Mean Accuracy} = \left(\frac{1}{n_{cl}}\right) \sum_i n_{ii}/t_i \quad (3.4)$$

$$\text{Mean IU} = \left(\frac{1}{n_{cl}}\right) \sum_i n_{ii}/(t_i + \sum_j n_{ji} - n_{ii}) \quad (3.5)$$

where n_{ii} is the number of pixels correctly predicted to be in class i , and n_{ij} is the number of pixels predicted to be in class i , while they actually belong to class j . n_{cl} is the number of predicted classes. $t_j = \sum_i n_{ij}$ is the total number of pixels that belong to class j .

Table 3.2 Segmentation Metrics.

Mean Accuracy	Overall Accuracy	Mean IU
94.4	92.3	63.4

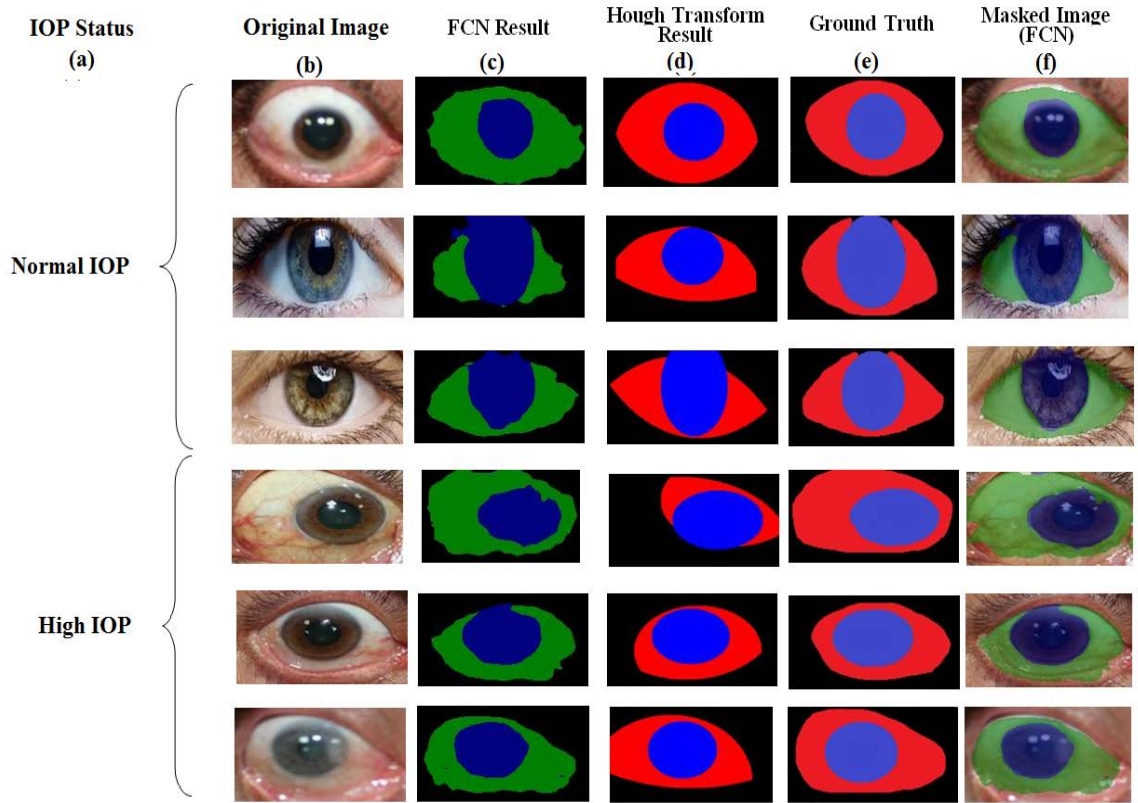


Figure 3.9. Sclera and Iris segmentation (a) IOP Status; (b) Original Image; (c) FCN Result; (d) Hough transform Result; (e) Ground truth; (f) Masked Image from FCN.

In [103], the segmentation technique focuses on eye area and eye landmarks detection. It relies on a shape model similar to the Active Shape Model (ASM) technique used for face landmarks detection. For sclera area detection, a look-up table is used based on the sclera color from the training images using a support vector machine (SVM) to generate the probability that a given pixel is a sclera or not. The technique is not suitable for sclera segmentation in our initial IOP screening framework since i) the shape model does not provide a good fit all the time (it may suffer from bad initialization), ii) the eyes used in our experiments have different color schema, and iii) the work focuses on detecting eye landmarks for facial expression detection (happy, sad, angry, etc.). This

requires the 6 landmarks of the eye, while our work will need further processing for pupil detection and other features from the sclera area.

In terms of computational complexity, FCN consists of multiple convolutional processes as a function of size and features, so the best complexity is $O(n \times m \times \log(m \times n))$, while the Hough transform, which was used in [100], has a best complexity of $O(n^3 \log(n))$ as a function of size of each dimension. The computational complexity of [103] depends on the algorithm used in the optimization process of the shape model + the complexity of the SVM, which is $O(\max(n, d), \min(n, d)^2)$, where n is the number of points and d is the number of dimensions. Taking into consideration that the proposed system is most competently designed for personal home use for IOP status detection (without professional/clinical assistance), using FCN will be a great choice, especially on the new neural processors utilized in modern smart-phones, which will reduce the execution time for the FCN compared to other techniques, that run over a regular CPU with higher complexity.

3.6 Feature Extraction

In this study, six features have been extracted from frontal eye images in order to detect the status of IOP, Iris/pupil ratio, MRL, RAP, Sclera Contour features (area, height or distance and angle). Two experiments have been applied. The first experiment has been applied over the whole sclera in order to extract the MRL, RAP, Contour Area and Contour Height features. The second experiment has been applied over a region of interest from the sclera in order to extract the MRL, RAP, Contour Area, Contour

Distance and Contour Angle features. For both experiments, the Pupil/Iris diameter ratio feature has been extracted through the same technique.

3.6.1 Pupil Iris Ratio

The Pupil/Iris diameter or radius ratio is measured once the Pupil and Iris have been detected from CHT. Figure 3.10 illustrates a sample of Pupil/Iris ratio results.

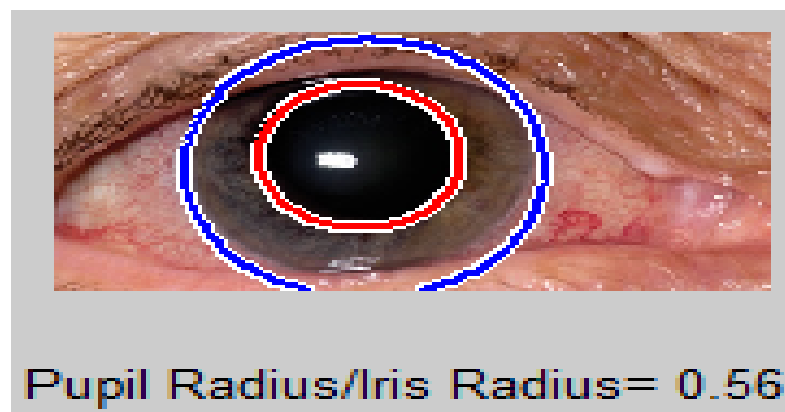


Figure 3.10 The ratio of Pupil/Iris.

3.6.2 MRL

The Mean Redness Level (MRL) feature is heavily based on the red pixel value. Each pixel is a combination of three values (Red, Green, and Blue). In addition, there are several cases that can result in reddish colors if we assign a large value to the red part of the pixel. Therefore, the red pixel value should always be larger than the green and blue pixel values. To prevent the pixel from being shifted to the yellow or violet colors, the difference between the green and the blue pixel values should not be too large.

Table 3.3 Ratio of Red Colors.

Color	RPV	GPV	BPV	MRL
Reddish1	255	200	200	0.477124
Reddish2	255	100	100	0.738562
Reddish3	255	50	50	0.869281
Pure Red	255	0	0	1
Reddish4	180	75	75	0.509804
Reddish5	180	50	50	0.575163
Reddish6	180	25	25	0.640523
Pure Dark Red	180	0	0	0.705882

As per Table 3.3, different ranges of the redness level of the eye are identified by the closest color to the pure red value. MRL can be calculated by the proposed formula in Equation 3.9:

$$\text{Mean of red pixels} = M(\text{RPV}) = M(S(:, :, 1)) = \sum_0^m S(:, :, 1) / m \quad (3.6)$$

$$\text{Mean of green pixels} = M(\text{GPV}) = M(S(:, :, 2)) = \sum_0^m S(:, :, 2) / m \quad (3.7)$$

$$\text{Mean of blue pixels} = M(\text{BPV}) = M(S(:, :, 3)) = \sum_0^m S(:, :, 3) / m \quad (3.8)$$

So,

$$\text{MRL} = \frac{3 \times M(\text{RPV}) - M(\text{GPV}) - M(\text{BPV})}{3 \times 255} \quad (3.9)$$

where $M(\text{RPV})$ corresponds to the mean of the red pixel values, $M(\text{GPV})$ is the mean of the green pixel values, $M(\text{BPV})$ is the mean of blue pixel values, and m refers to the total number of pixels in the extracted sclera.

3.6.2.1 MRL - First Experiment - Whole Sclera

After extracting the whole sclera using CHT (Section 3.4), The MRL equation has been applied over the whole sclera as shown in Figure 3.11.

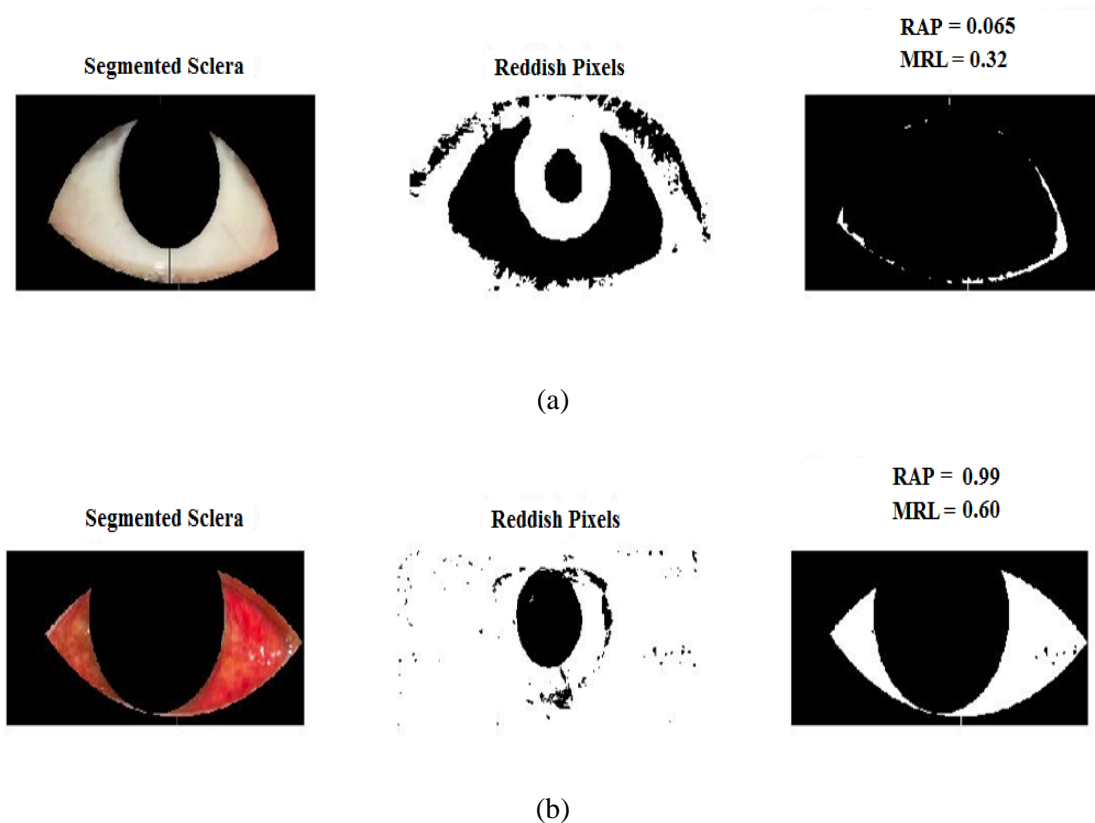


Figure 3.11 Results of MRL and RAP for (a) Normal and (b) High IOP.

3.6.2.2 MRL - Second Experiment - Part of the Sclera

After cropping a targeted portion of the sclera, extended from two horizontal lines at one third and half of the lower vertical radius of the Iris (Figure 3.12 (a)), the MRL feature has been calculated (Figure 3.12 (b)).



Figure 3.12 Extracting sclera and calculating MRL/RAP features.

The MRL features are calculated from Image (S) from the extracted portion of the sclera. This portion is created by constructing a black image that has the same size of the merged extracted portions of the sclera which is Image (S), as shown in Figure 3.12 (b). Then, the colored image is scanned pixel by pixel. Every time a red value is located, the black image pixel value is modified into a white pixel value.

3.6.3 RAP

The Red Area Percentage (RAP) feature is defined as the mean of the red pixel percentage in the binary image of the extracted sclera (P).

$$RAP = \left(\sum_{i=0}^n P_i \right) \div m \quad (3.10)$$

In Equation (3.10), P_i represents the red pixel values in the extracted sclera, and m represents the total number of pixels in the extracted sclera. Figure 3.10 represents samples of our MRL and RAP results.

3.6.3.1 RAP - First Experiment - Whole Sclera

Once the whole sclera has been extracted using CHT (section 3.4), RAP has been measured over the whole sclera as shown in Figure 3.11.

3.6.3.2 RAP - Second Experiment - Part of the Sclera

After cropping a targeted portion of the sclera, extended from two horizontal lines at one third and half of the lower vertical radius of the Iris (Figure 3.12 (a)), the RAP feature has been calculated (Figure 3.12 (b)). Similar to MRL, the RAP feature is calculated from Image (S).

3.6.4 Sclera Contour Features

The idea of measuring features of the contour of the sclera is inspired by sonar techniques such as ultrasound where active trained operators/healthcare personnel are involved [104]. In order to obtain the contour of the sclera, first, the “Activecontour” [105] function is employed in which the 2-D grayscale image is segmented into foreground (object) and background regions using the active contour based segmentation. The black and white (bw) output image is a binary image where the foreground is white (logical true) and the background is black (logical false).

3.6.4.1 Contour Features (Area, Height) - First Experiment - Whole Sclera

In these computations, the mask is a binary image that specifies the initial state of the active contour. The boundaries of the object region(s) (white) in the mask define the

initial contour position in order to segment the image, as shown in Figure 3.13. To obtain faster and more accurate segmentation results, we specify an initial contour position that is close to the desired object boundaries.

To find the area and height of the contour, the “regionprops” function is used. The area can be derived directly from this function, and the height can be calculated by subtracting the upper extreme and the lower extreme. The area is then divided by the mask area to get the area ratio and similarly the height is divided by the mask height to obtain the height ratio. These are newly proposed features from frontal eye images in our work that have not been previously investigated in the literature for IOP risk assessment.



Figure 3.13 Active contour.

3.6.4.2 Contour Features (Area, Distance, Angle) - Second Experiment

The idea of measuring three features from the extracted contour of the sclera is also inspired by sonar techniques such as ultrasound where traditionally, the thickness of the cornea liquid is measured by active trained operators/healthcare personnel who scan

certain points of the eye [104]. The newly proposed strategy is automated and works by scanning the area of the eye shown in Figure 3.14, where the contour is extracted using the active contour model [103] to calculate the Distance (D), Angle (α), and Area. These are newly proposed features from frontal eye images that have not been previously investigated in the literature for IOP.

To automatically compute the D, α and Area measures, as shown in Figures 3.14 and 3.15, the triangle consisted of points P1, P2, P3 with three sides a, b, and D is considered. The height (h), Area, and angle (α) can be found from the triangle. The coordinates of points P1 and P2 can be found from the border of the Iris for the left and right eyes. P1 and P2 have the same coordinates at the starting point at 0° of the Iris perimeter. By moving 120° and 70° counterclockwise on the perimeter of the Iris, point P1 for the left and right eyes, respectively can be found and by moving 120° and 70° clockwise on the perimeter of the Iris, point P2 for the left and right eyes, respectively, can be identified, as described in Equations 3.11-3.16. The two angles for the left eye and right eye from the side of the nose are chosen because after a number of experiments, the results show that this side extracts most of the sclera and guaranteed to include most parts of the sclera. Selecting larger or smaller areas would result in including part of the skin or excluding parts of the sclera. Moreover, P3 is also a known point from the horizontal line illustrated in the MRL section, which is the midpoint between the left/right border of the image and the left/right border of the Iris for the left and right eyes (Equations 3.17-3.19).

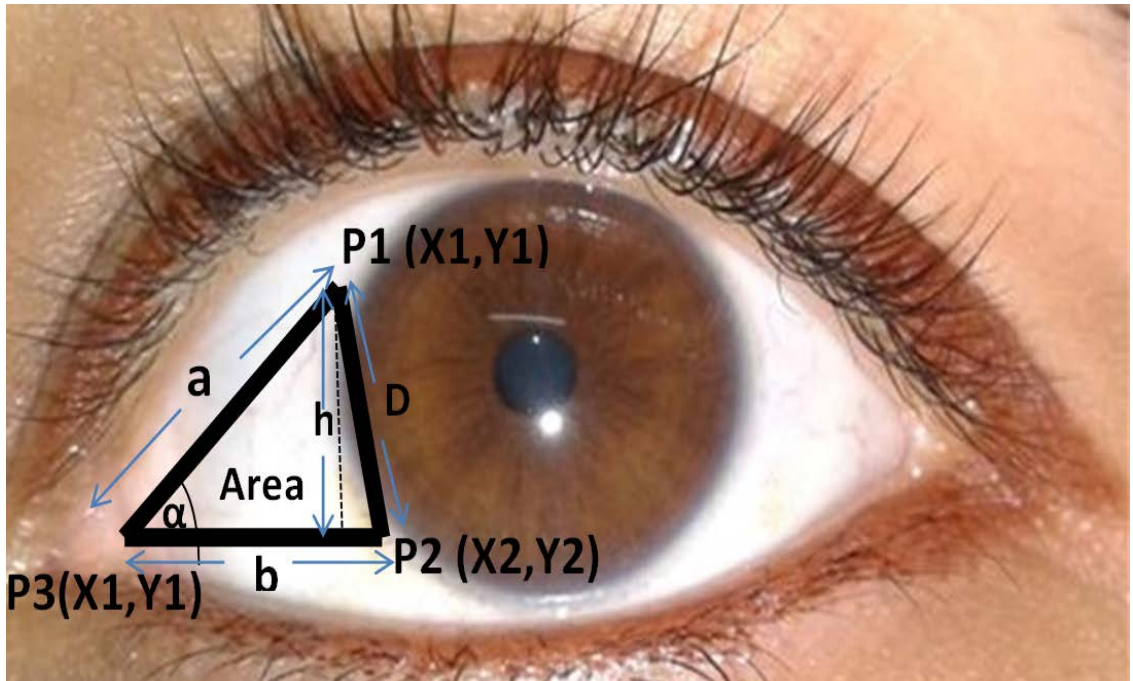


Figure 3.14 Depiction of Distance (d), Angle (α) and Area features of the contour of the sclera.

$$P_1 = (P_{x1}, P_{y1}) \quad (3.11)$$

where,

$$P_{x1} = col_i - \sqrt{r_i^2 - \left(\frac{r_i}{2}\right)^2} \quad (3.12)$$

$$P_{y1} = row_i - \frac{r_i}{2} \quad (3.13)$$

and,

$$P_2 = (P_{x2}, P_{y2}) \quad (3.14)$$

where,

$$P_{x2} = \frac{col_i - r_i}{2} \quad (3.15)$$

$$P_{y2} = row_i + \frac{r_i}{2} \quad (3.16)$$

and,

$$P_3 = (P_{x3}, P_{y3}) \quad (3.17)$$

where,

$$P_{x3} = col_i - \sqrt{r_i^2 - \left(\frac{r_i}{2}\right)^2} \quad (3.18)$$

$$P_{y3} = \frac{row_i + 2}{3r_i} \quad (3.19)$$

where r_i is the radius of the Iris, and row_i and col_i represent the coordinates of the center of the Iris.

After identifying the coordinates of points P1, P2 and P3, Equations 3.20-3.24 depict the steps to compute the three sclera contour features Distance (D), Angle (α) and Area. The length of the side P1P2 (which is D) is almost the same size of the diameter of the Iris after applying Equation 3.22. The height (h) can be found by moving pixel by pixel from the coordination of point P1 across the y axis until reaching the base (b). Once we reach the base (b), the coordination is known and the length of the height (h) is calculated. The Angle (α), and Area can thus be computed from Equations 3.23 and 3.24.

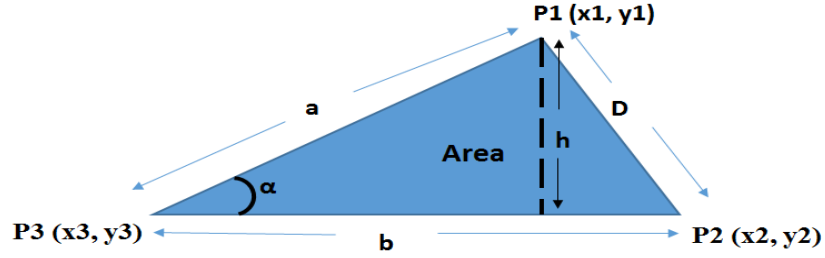


Figure 3.15 Distance (D), Angle (α) and Area measurements.

$$a = \sqrt{((P_{x3} - P_{x1})^2 + (P_{y3} - P_{y1})^2)} \quad (3.20)$$

$$b = \sqrt{((P_{x2} - P_{x3})^2 + (P_{y2} - P_{y3})^2)} \quad (3.21)$$

$$D = \sqrt{((P_{x2} - P_{x1})^2 + (P_{y2} - P_{y1})^2)} \quad (3.22)$$

Therefore,

$$\alpha = \text{Sin}^{-1} \frac{h}{a} \quad (3.23)$$

and,

$$\text{Area} = \frac{a.b.\text{Sin}(\alpha)}{2} \quad (3.24)$$

3.7 Feature Representation

Once we extracted all the features from the images, the results were stored in a features matrix. The matrix consists of multiple rows that correspond to the number of features and four hundred columns ($n=400$) that correspond to the number of images in the database used in this study.

3.7.1 Feature Representation for the First Experiment

The features representation matrix for the first experiment is shown in Figure 3.16.

$$\begin{bmatrix}
 \frac{\text{Pupil (1)}}{\text{Iris (1)}} & \frac{\text{Pupil (2)}}{\text{Iris (2)}} & \dots & \frac{\text{Pupil (n)}}{\text{Iris (n)}} \\
 \text{RAP (1)\%} & \text{RAP (2)\%} & \dots & \text{RAP (n)\%} \\
 \text{MRL (1)} & \text{MRL (2)} & \dots & \text{MRL (n)} \\
 \frac{\text{Contour Area(1)}}{\text{Mask Area(1)}} & \frac{\text{Contour Area (2)}}{\text{Mask Area(2)}} & \dots & \frac{\text{Contour Area (n)}}{\text{Mask Area(n)}} \\
 \text{Contour Height (1)} & \text{Contour Height (2)} & \dots & \text{Contour Height (n)} \\
 \text{Mask Height(1)} & \text{Mask Height(2)} & \dots & \text{Mask Height(n)}
 \end{bmatrix}$$

Figure 3.16 Features matrix for the first experiment.

3.7.2 Feature Representation for the second experiment

The features representation matrix for the second experiment is shown in Figure 3.17.

$$\begin{bmatrix}
 \frac{\text{Pupil (1)}}{\text{Iris (1)}} & \frac{\text{Pupil (2)}}{\text{Iris (2)}} & \dots & \frac{\text{Pupil (n)}}{\text{Iris (n)}} \\
 \text{RAP (1)\%} & \text{RAP (2)\%} & \dots & \text{RAP (n)\%} \\
 \text{MRL (1)} & \text{MRL (2)} & \dots & \text{MRL (n)} \\
 \frac{\text{Contour Area(1)}}{\text{Iris Area}} & \frac{\text{Contour Area(2)}}{\text{Iris Area}} & \dots & \frac{\text{Contour Area(n)}}{\text{Iris Area}} \\
 \text{Contour Distance(1)} & \text{Contour Distance(2)} & \dots & \text{Contour Distance(n)} \\
 \text{Iris Radius} & \text{Iris Radius} & \dots & \text{Iris Radius} \\
 \text{Contour angle (radion)(1)} & \text{Contour angle (radion)(2)} & \dots & \text{Contour angle (radion)(n)}
 \end{bmatrix}$$

Figure 3.17 Features matrix for the first experiment.

3.8 Classification

Once all features extracted and stored in the dataset, various classification techniques are applied to select the most appropriate machine learning algorithm with respect to time and accuracy. In this study, two experiments have been conducted and machine learning algorithms have been applied in each experiment.

3.8.1 First Experiment

Several machine learning algorithms were applied on the extracted features to detect the status of IOP. For instance, support vector machine SVM was tested using the radial basis function (RBF) kernel along with neural network classifier [106, 107] to pick the best accuracy. Neural network classifier shows the best accuracy and execution time over SVM. Therefore, the neural network classifier has been used in the rest of this experiment. The neural network-based classification applied to the extracted features is designed using the following settings.

Three network layers have been utilized for the classification purpose. The first layer is the input layer which has five inputs corresponding to the number of features; the second layer is one hidden layer that contains 10 nodes, and finally there is one output layer that shows the final binary result (normal or high eye pressure). When the input values are moved from one layer to another, they get multiplied by weights and this procedure is repeated all the way to the output layer. The hidden layer values may be greater than 1, less than zero or in between. Therefore, in our research, we used the

sigmoid as an activation function to adjust and scale all the results to be between 0 and 1 for the output of each node.

Finally, in this framework if the output layer has a value of 0.5 or greater, it will be considered as high eye pressure; otherwise it will be considered as normal eye pressure. Hence, the final output of our framework is either normal or high IOP. We applied 75% of the images in the database for training and 25% for testing. The patient images used in the testing phase are completely different from the ones used in the training phase (not different images from the same patients, but different images for different patients).

3.8.2 Second Experiment

Several machine learning algorithms were applied on the extracted features. For instance, support vector machine (SVM) was tested along with the Decision Tree (DT) classifier to pick the best accuracy. For SVM, different kernels have been utilized, but only the radial basis function (RBF) kernel would converge. In this work, the decision tree classifier shows better accuracy over SVM. Therefore, DT has been used in the rest of this experiment. 75% of the eye images in the database are utilized for training and validation and 25% are used for testing the classifiers. The patient images used in the testing phase are also completely different from the ones used in the training phase (not different images from the same patients, but different images for different patients). The binary decision tree classifier is applied to the six extracted features using the CART (Classification And Regression Tree) algorithm [108]. The output design of the tree with

the following settings yielded the best results over several testing structures. The total number of nodes is 31 arranged in 6 layers of depth. The final output of our framework is either normal or high IOP.

CHAPTER 4: IMPLEMENTATION AND TEST PLAN

The objective of this study is to determine the status of the patients that have high eye pressure. Therefore, a set of features were studied to achieve this objective. Six features are targeted to determine the status of IOP. The whole six features are Pupil/Iris Ratio, RAP, MRL, Contour Height or Distance, Contour Area and Contour Angle. The implementation is carried out by MATLAB 2014a software as shown in Figure 4.1. The first feature is measuring the diameter of the pupil. Clinically, the diameter of the pupil is measured in millimeters. However, dealing with images produces results in pixels. Therefore, we use the Iris to calculate the ratio between the Pupil and the Iris to have consistent results in computer vision and image analysis. The other five features are extracted from the sclera. However, the extraction of the sclera is carried out in two different ways. Therefore, two experiments were designed based on the sclera segmentation. The first experiment extracted the sclera by using the CHT technique. The feature include RAP (the average of the red pixels in the region of interest of the sclera), MRL (which calculates the nature of the redness color since high IOP and Glaucoma candidates have red eyes in the sclera area), Contour Height and Contour Area features measured based on the whole sclera, as shown in Figure 4.2. It is important to mention that idea of the contour features have been adopted from the sonar technique applied on eye images. The sonar technique counts on three features 1) the Angle (α) 2) the Area and

3) Distance between two specific points (P1 and P2) (AOD) as shown in Figure 4.3, where AOD, TIA and TISA in the Figure refer to Angle-Opening Distance, the Trabecular-Iris Angle, and the Trabecular-Iris Space Area, respectively. These are substituted in this study by Contour Distance, Contour Angle, and Contour Area, respectively. The contour features are measured by using the Haar filter and active contour model techniques. In the second experiment, the sclera has been extracted by using a designed FCN. RAP and MRL are measured from the rectangular shape region of interest from the sclera, and the contour features are measured from the triangular shape region of interest from the sclera. After extracting all features from the eye images, a test is applied on the results by creating a database and storing all results that came from the features. Once all the features have been measured and stored, classification techniques are applied to train and test the images in order to detect the status of IOP. Various classification techniques were applied for both experiments. For the first experiment, SVM and NN are applied to train and test the images. For the second experiments, SVM and DT are applied to train and test the images and resulting features in order to detect the status of IOP.



Figure 4.1 MATLAB Software 2014a.



Figure 4.2 Whole sclera extracted.

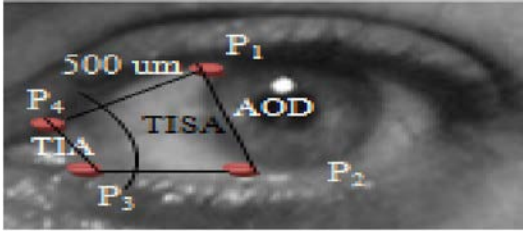


Figure 4.3 Contour features adopted from sonar.

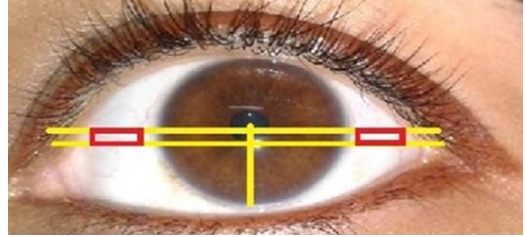


Figure 4.4 MRL and RAP Region of Interest.

CHAPTER 5: RESULTS

The objective of our study is to extract features from frontal eye images in an effort to determine the status of IOP (normal or high). We initially demonstrate the results that came from each feature.

5.1 First experiment

5.1.1 Pupil/Iris Ratio

During the day, the normal adult Pupil/Iris diameter range varies (between 2mm to 4mm for the Pupil and 11mm to 14mm for the Iris [109]). Traditionally, the radius of the Iris and Pupil is measured in millimeters. However, according to computer vision, it is inaccurate to represent the radius in millimeters even when images contain information such as fixed distance and tangible objects. Therefore, in this study, we rely on both the Iris and the Pupil to calculate the ratio for accurate results because the units will be discarded. In our study, the ratio of the Pupil/Iris in daytime hours fall between (0.5, 0.7) for adults. Table 5.4 represents a sample of the results after our Pupil/Iris ratio detection technique was applied to the normal and high IOP cases. The table is extended to include other features as well. The table is split into two blocks; normal and high IOP. Each block is further split into five blocks, corresponding to each feature (Pupil/Iris ratio, MRL,

RAP, Contour Area and Contour Height). The mean and standard deviation (STD) and median values are also reported in the last two rows.

The results show that there is a strong relationship between the Pupil/Iris ratios and high intraocular pressure. Once the medical community has this knowledge, we believe that our smart framework will help in the initial screening of IOP that may lead to early detection of high IOP in an effort to circumvent the onset of blindness.

5.1.2 MRL and RAP

The extraction of the sclera was the most difficult part of this research, since the sclera shares the same features of the skin. The sclera was extracted, and the Mean Redness Level was calculated according to the proposed Equation 3.9. Red Area Percentage was also calculated in the extracted sclera, as shown in Equation 3.10. Table 5.4 also contains a sample of the results for normal and high IOP cases based on MRL and RAP measures. The results show that there is a strong relationship between the MRL, RAP and IOP. This information will, also, aid in automatic IOP screening for early detection of high risk IOP, in an effort to help in preventing the blindness.

5.1.3 Contour Features (Area, Height)

In this section of the results, we report the sclera contour area and height measures for normal and high eye pressure cases from frontal eye images. Table 5.4 depicts these results as well. The sclera contour features values are also represented as ratios, as described in the previous section.

5.1.4 High Risk IOP Determination

The system was prepared based on the settings of neural network classifier stated in last section. The status of the eye (normal or high IOP) came from the activation function of the neural network implementation. The implementation dictates the type of normalization functions that can be used to bring the activation values in the range between 0-1. These computations are done in a fashion that sums up all the percentages to 1. For example, higher values of the Pupil/Iris ratio could relate to having a higher value in the range close to 1. It is important to note that however, the system does not count on one feature to make the final decision, and rather depends on five features altogether along with a neural network machine learning model to provide the final decision. The value 0.5 from the output range is used as a cutoff to differentiate between normal and high IOP. As an example, when the Pupil/Iris ratio was equal to 0.7, the resulted scaled value was high and close to 1. This indicates that if the other features of the same eye image also result in a high value from the range [0-1], the eye status is likely to be classified as high IOP.

Tables 5.1 and 5.2 show the test phase confusion matrix for neural network (NN) and SVM respectively, regarding the proposed framework. The table is split according to the status of eye pressure (Normal, High pressure). At the beginning, the data was shuffled, then, 65% of the eye images were taken randomly for the training phase, 25% was taken for the testing phase and 10% for validation. The technique was run at least 10 times and the average values were recorded. We have shown the accuracy of the classifier, when properly trained and validated, for identifying high IOP cases using the

five features from frontal eye images. In this work, NN was adopted as it provided better accuracy, and hence it is the focal classifier.

Table 5.1 Test Confusion Matrix for neural network

	<i>Normal</i>	<i>High Pressure</i>	
<i>Normal</i>	49	3	
<i>High Pressure</i>	1	47	
<i>Accuracy</i>	98.0%	94.0%	Overall Acc. 96.0%
<i>Error</i>	2.0%	6.0%	Overall Err. 4.0%

Table 5.2 Test Confusion Matrix for SVM

	<i>Normal</i>	<i>High Pressure</i>	
<i>Normal</i>	45	6	
<i>High Pressure</i>	5	44	
<i>Accuracy</i>	90.0%	88.0%	Overall Acc. 89.0%
<i>Error</i>	10.0%	12.0%	Overall Err. 11.0%

There are 200 images in the database that correspond to normal eye pressure. The 65% training consists of 130 random images representing normal eye pressure and 130 random images representing high eye pressure images. The 25% testing data consists of 50 random images that represent the normal eye image, and 50 random images representing high eye pressure. The 10% validation data consist of 20 random images. The proposed framework using NN was able to detect 49 normal eye images as normal pressure, and 1 image that corresponds to normal eye pressure was detected as high eye pressure. The accuracy for normal eye pressure is 98.0%.

The second column represents the high eye pressure cases, and there are 50 images in the test phase that correspond to high eye pressure. The proposed framework detected 3 high eye pressure images as normal pressure, and 47 high eye pressure images as high eye pressure, so the accuracy for the high eye pressure is 94.0%. As shown in the confusion matrix table, the overall accuracy (Acc.) for the proposed framework is 95.0% and 5.0% corresponds to the overall error (Err.).

The performance of a classifier can be determined by computing the accuracy, sensitivity and specificity using TP, FP, FN and TN values, where TP refers to true positives, TN is true negatives, FP is false positives and FN is false negatives. The equations of accuracy, sensitivity and specificity are shown below [110-112]:

$$\text{Accuracy} = \frac{(TP+TN)}{(TP+FP+TN+FN)} \quad (5.1)$$

$$\text{Sensitivity} = \frac{TP}{(TP+FN)} \quad (5.2)$$

$$\text{Specificity} = \frac{TN}{(TP+FN)} \quad (5.3)$$

According to Equations 5.1-5.3, the accuracy value is 0.95, the sensitivity value for the proposed framework is 0.95 and the specificity value is 0.97.

The system used the adaptive learning rate as shown in Figure 5.1. We found these as the optimal specifications yielding best performances for our neural network; as they were determined after several experiments.

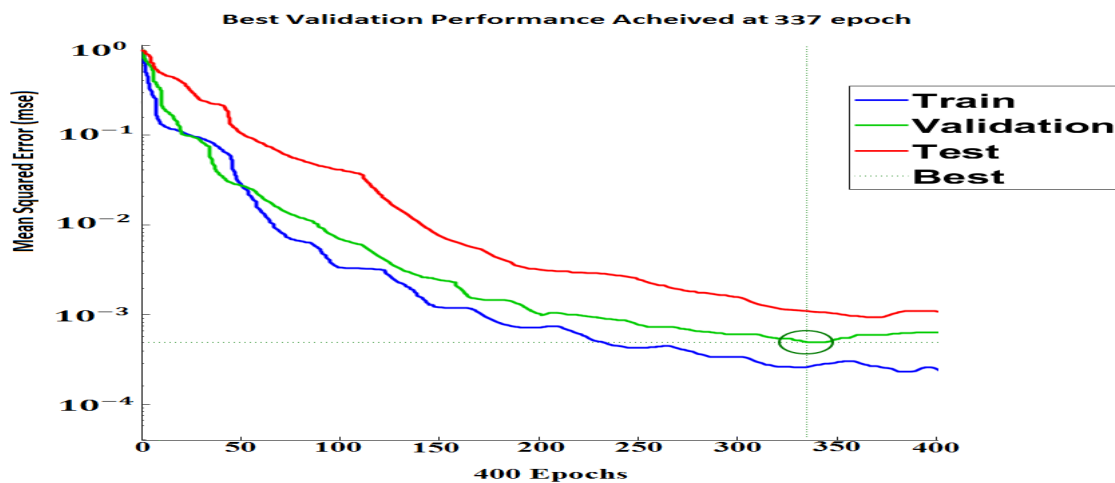


Figure 5.1 Training and testing performance.

Another classifier was applied and tested using only the MRL, contour height and contour area features, as shown in Table 5.3 (without Pupil/Iris ratio and RAP features).

Table 5.3 Test Confusion Matrix for neural network with three features (MRL, contour area, and contour height).

	<i>Normal</i>	<i>High Pressure</i>	
<i>Normal</i>	45	5	
<i>High Pressure</i>	1	40	
<i>Accuracy</i>	98.2%	88.9%	Overall Acc. 94.0%
<i>Error</i>	1.8%	11.1%	Overall Err. 6.0%

As shown in Tables 5.1 and 5.3 the performance of the five features classifier outperforms the one trained with three features only.

Table 5.4 Sample Values of Pupil/Iris Ratio, MRL, RAP and Contour features (Area, Height) Results for Normal, High Eye Pressure

Normal IOP					High IOP				
Pupil/Iris Ratio	RAP	MRL	Contour Area	Contour Height	Pupil/Iris Ratio	RAP	MRL	Contour Area	Contour Height
0.3600	0.1612	0.2937	0.4403	0.6733	0.8556	0.9922	0.6605	0.2595	0.3533
0.3488	0.0710	0.2197	0.5413	0.5267	0.6627	0.9945	0.6059	0.1181	0.3119
0.3774	0.3670	0.3396	0.4485	0.6000	0.6875	0.8143	0.4025	0.3031	0.4833
0.5833	0.4961	0.2319	0.5755	0.8200	0.7600	0.6066	0.6025	0.0622	0.4000
0.3833	0.2269	0.2449	0.5480	0.7444	0.5208	0.7050	0.6536	0.2371	0.2400
0.4182	0.4472	0.3667	0.4730	0.6867	0.7651	0.6582	0.5020	0.2760	0.3000
0.4545	0.0978	0.1757	0.4704	0.7000	0.7310	0.7775	0.6874	0.1299	0.3267
0.4909	0.3499	0.3371	0.4877	0.7933	0.8000	0.5319	0.5493	0.3546	0.2467
0.5000	0.3352	0.2545	0.5819	0.7800	0.6167	0.6075	0.7139	0.3622	0.4133
0.3968	0.4782	0.2007	0.4735	0.6689	0.4792	0.1927	0.6240	0.0632	0.1467
0.3077	0.1925	0.368	0.4935	0.6067	0.6181	0.6663	0.6313	0.1977	0.3000
0.3333	0.0733	0.1416	0.4059	0.7933	0.5556	0.8798	0.5975	0.0594	0.2655
0.2727	0.2183	0.2955	0.4198	0.6800	0.6872	0.8236	0.7031	0.2650	0.3733
0.4182	0.3283	0.2306	0.5174	0.6533	0.7792	0.9174	0.5050	0.1474	0.4324

0.5032	0.0978	0.2449	0.5480	0.7444	0.7263	1.0000	0.6915	0.2359	0.2467
.
.
.
<i>Mean</i>	<i>Mean</i>	<i>Mean</i>	<i>Mean</i>	<i>Mean</i>	<i>Mean</i>	<i>Mean</i>	<i>Mean</i>	<i>Mean</i>	<i>Mean</i>
0.4491	0.3506	0.2807	0.4553	0.6134	0.6983	0.8550	0.6363	0.2013	0.3147
<i>STD</i>	<i>STD</i>	<i>STD</i>	<i>STD</i>	<i>STD</i>	<i>STD</i>	<i>STD</i>	<i>STD</i>	<i>STD</i>	<i>STD</i>
0.0924	0.1165	0.0677	0.0722	0.1260	0.1010	0.2672	0.0732	0.1182	0.1574
<i>Median</i>	<i>Median</i>	<i>Median</i>	<i>Median</i>	<i>Median</i>	<i>Median</i>	<i>Median</i>	<i>Median</i>	<i>Median</i>	<i>Median</i>
0.4100	0.2320	0.2795	0.4673	0.6451	0.6737	0.6963	0.6984	0.2276	0.3000

5.2 Second Experiment

In this study, an initial IOP risk assessment framework is developed based on frontal eye images. A fully convolutional network is proposed in the framework for sclera and iris segmentation. From these segmented areas, the Pupil/Iris diameter ratio, the Mean Redness Level (MRL), the Red Area Percentage (RAP) features along with three other proposed sclera contour features (distance, area and angle) are extracted. The final results of the risk grade level of IOP are based on machine learning techniques using decision tree and support vector machine classifiers. The implementation is carried out by MATLAB 2014a software.

5.2.1 Pupil/Iris Ratio

The results in Table 5.5 indicate that there is a strong relationship between the Pupil/Iris ratios and high intraocular pressure. This technique will help in the initial

screening of IOP that may lead to early detection of high IOP in an effort to circumvent the onset of blindness.

5.2.2 MRL and RAP

The extraction of the sclera was the most difficult part of this research, since the sclera shares the same features of the skin. A specific part of the sclera was extracted, and the Mean Redness Level was calculated according to the proposed Equation 3.9. Red Area Percentage was also calculated as the average of the red pixels in the extracted part of the sclera, as shown in Equation 3.10.

Table 5.5. Sample of Pupil/Iris Ratio, MRL and RAP Feature Values for Normal and High IOP Cases

<i>Normal</i>			<i>High pressure</i>		
Pupil/Iris Ratio	MRL	RAP	Pupil/Iris Ratio	MRL	RAP
0.53	0.13	0.32	0.81	0.56	0.86
0.59	0.11	0.27	0.79	0.57	0.76
0.55	0.08	0.06	0.80	0.63	0.86
...
<i>AVG for 200 IMAGES= 0.45</i>	<i>AVG for 200 IMAGES= 0.29</i>	<i>AVG for 200 IMAGES= 0.19</i>	<i>AVG for 200 IMAGES= 0.70</i>	<i>AVG for 200 IMAGES=0.69</i>	<i>AVG for 200 IMAGES= 0.84</i>

Table 5.5 also contains a sample of the results for normal and high eye pressure cases based on the MRL and RAP features, numerically. The results show that there is a big difference between normal cases and cases with high eye pressure. This information will also, aid in automatic IOP screening for early detection of IOP in an effort to help in preventing the blindness.

5.2.3 Contour Features (D, α , and Area)

In this section of the results, we report the D, α , and Area feature values of the sclera contour for normal and high eye pressure cases from frontal eye images of the database. Table 5.6 depicts these results.

Table 5.6. Contour of the Sclera Feature Values for Normal and High Intraocular Pressure Cases

<i>Normal</i>			<i>High pressure</i>		
<i>D</i>	<i>Area</i>	<i>α</i>	<i>D</i>	<i>Area</i>	<i>α</i>
<i>(Contour Distance/Iris radius)</i>	<i>(Contour Area/Iris Area)</i>	<i>(Radion)</i>	<i>(Contour Distance/Iris radius)</i>	<i>(Contour Area/Iris Area)</i>	<i>(Radion)</i>
<i>0.0690</i>	0.9844	0.6511	0.0132	0.1232	0.0234
<i>0.0569</i>	0.7466	0.8380	0.0148	0.3466	0.1343
<i>0.0872</i>	0.6415	0.6450	0.0230	0.0324	0.5622
<i>0.0725</i>	0.7454	0.7581	0.0262	0.0734	0.0324
<i>0.0501</i>	0.7058	0.6248	0.0362	0.0973	0.0231
...
<i>AVG for 200 images = 0.0723</i>	AVG for 200 images = 0.7129	AVG for 200 images = 0.7387	AVG for 200 images = 0.0178	AVG for 200 images = 0.1079	AVG for 200 images = 0.1588

5.2.4 IOP Risk Determination

Once we extracted all six features from the images, a binary classifier is applied to the extracted features in order to classify the images for an initial screening of IOP risk assessment by distinguishing normal from high IOP.

After applying the decision tree, a loss of 0.0615 has been achieved with 10-fold cross validation. The constructed decision tree structure is depicted in Figure 5.2. These

noted specifications yield the best performances and accuracies over several trials and experiments. Figures 5.3 (a) and (b) represent two samples, one with normal eye pressure and another with high eye pressure based on clinical ground-truth, and after applying the proposed techniques to the eye images. The results show that the system was able to provide a highly correlated outcome. The proposed framework shows a strong relationship between the extracted frontal eye image features and IOP. This information will help in the early assessment of IOP. The framework is fully automated. Once the user inserts an image, the FCN segmentation is performed, all features are extracted and the status of IOP will be calculated. The final result “Status of IOP” comes from the DT classifier.

The final optimum structure of the used decision tree (DT) is shown in Figure 5.2. Taking a deep look to this output gives an idea about the most efficient features from the introduced ones. As shown in Figure 5.2, the most important feature is feature number 6 (x6 in the figure), which is the Contour Angle. The next important feature is the RAP (Red Area Percentage) which is marked x2 in the Figure. Then, x1 and x4 come next which are the Pupil/Iris ratio and Contour Distance features, respectively. All other features have been also used but only to fine tune the classifier and in some cases they can be removed completely and only x1, x2, x4, and x6 are used in the classification process. This perspective is also consonant with the correlation graphs shown in Figure 5.4. As can be easily observed from Figure 5.4, the Contour Angle feature can smoothly separate high and normal IOP with minimum error. After the Contour Angle feature, the RAP feature and then Pupil/Iris ratio and the Contour Distance feature can be used to

distinguish the two classes. Actually, this variation in features gives an advantage to DT over SVM because DT can override some features for the most important ones, unlike SVM, which tries to use all given features even with small weights.

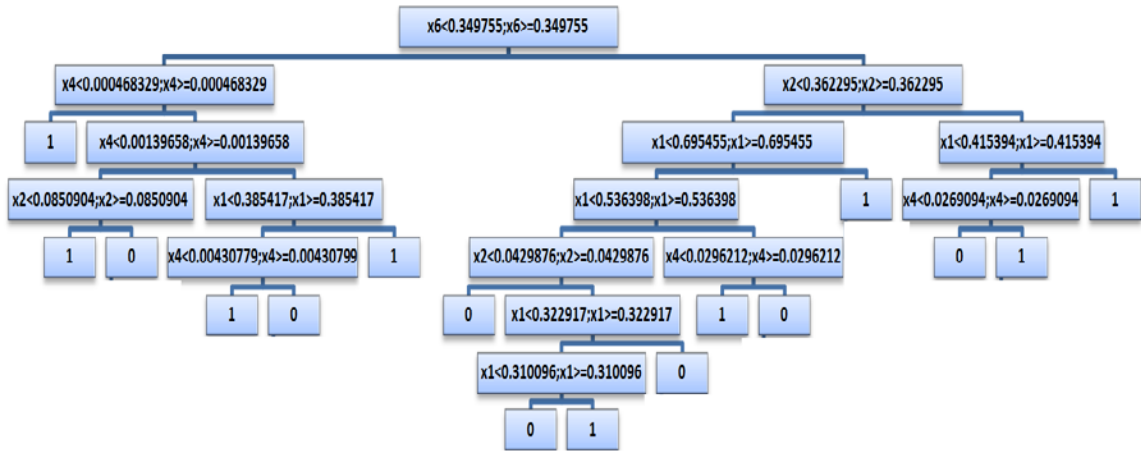


Figure 5.2 The Constructed Decision Tree.

The confusion matrices for the proposed framework that came out from the Decision Tree and Support Vector Machine classifiers, respectively, are presented in Tables 5.7-5.11. The accuracy results have been improved from 80.25% in [102] using Hough transform for sclera segmentation to over 97% using FCN segmentation when the same features are applied. The tables are split according to the status of eye pressure (Normal, High pressure). At the beginning, the data is mixed and shuffled, then, 65% of the eye images in the database are taken for training, 10% for validation, and 25% are taken for testing. These percentages are not taken from each group separately, but have been chosen from the total image population to allow for completely random sampling in the training, validation and test groups. The results show that decision tree provides

higher accuracy than SVM. Therefore, the decision tree classifier has been adopted in this research.

Table 5.7. Training Phase Confusion Matrix for DT 65% of the data

	Normal	High Pressure	
Normal	123	3	
High Pressure	2	132	
Accuracy	98.4%	97.8%	Overall Acc.: 98.1%
Error	1.6%	2.2%	Overall Err.: 1.9%

Table 5.9. Test Phase Confusion Matrix for DT 25% of the data

	Normal	High Pressure	
Normal	55	1	
High Pressure	2	42	
Accuracy	96.49%	97.67%	Overall Acc.: 97.08%
Error	3.5%	2.3%	Overall Err.: 2.9%

Table 5.8. Validation Phase Confusion Matrix for DT 10% of the data

	Normal	High Pressure	
Normal	18	1	
High Pressure	0	21	
Accuracy	100.0%	95.45%	Overall Acc.: 97.73%
Error	0%	4.5%	Overall Err.: 2.25%

Table 5.10 Overall Confusion Matrix for DT 100% of the data

	Normal	High Pressure	
Normal	196	5	
High Pressure	4	195	
Accuracy	98.0%	97.5%	Overall Acc.: 97.75%
Error	2.0%	2.5%	Overall Err.: 2.25%

Table 5.11 Overall Confusion Matrix for SVM

	Normal	High Pressure	
Normal	188	14	
High Pressure	12	186	
Accuracy	94.0%	93.0%	Overall Acc.: 93.5%
Error	6.0%	7.0%	Overall Err.: 6.5%

There are 400 eye images in the database that were split into two parts. According to Table 5.10, for the overall data, 200 eye images represent normal eye pressure cases. The system was able to detect all 196 eye images as normal and 4 normal eye images as high eye pressure. The accuracy of the normal phase is 98%. There are also 200 eye images in the dataset that represent high eye pressure cases. The system was able to detect 195 eye images as high eye pressure and 5 eye images as normal eye pressure. The accuracy of the high eye pressure phase is 97.5%. The overall accuracy is 97.75% and the overall error is 2.25%, as shown in Table 5.10.

For further analysis, Figure 5.4 shows the correlation between the frontal eye features and clinical mmHg measurements of IOP. The X-axis represents the feature value of Pupil/Iris ratio for part (a), red area percentage for part (b), MRL for part (c), contour distance ratio for part (d), contour area ratio for part (e), and contour angle ratio (α) for part (f). The Y-axis represents the actual IOP value in mmHg that corresponds to each eye with the given features. As shown in the Figure, the Pupil/Iris ratio, RAP and MRL features are directly proportional to the IOP values in mmHg, while the sclera contour features (distance, area and angle) are inversely proportional to IOP.

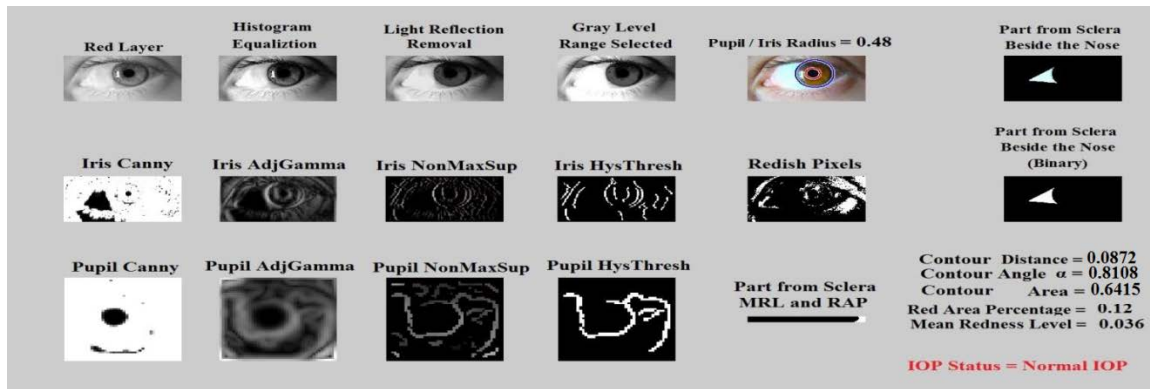
The curve fitted graphs for IOP values versus the features are also shown as an exponential trend in each of the six parts of Figure 5.4 using regression models. Figure 5.3 also shows the results that came out from the proposed framework for normal eye pressure (a) and high eye pressure (b). The Figure shows the preprocessing steps along with the extracted region of interest (Iris, Pupil, part of sclera for MRL and RAP, Part of

sclera for Contour features). Moreover, the Figure shows the values corresponding to each feature. For the purpose of classification, the contour features have been normalized as the following:

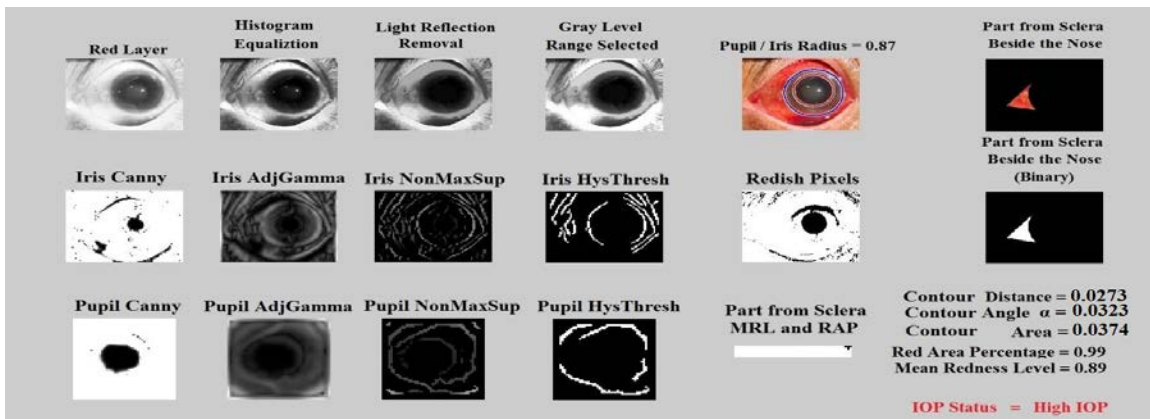
$$\text{Contour Distance} = \frac{\text{Contour Distance}}{\text{Iris Radius}} \quad (5.4)$$

$$\text{Contour Area} = \frac{\text{Contour Area}}{\text{Iris Area}} \quad (5.5)$$

Contour Angle values cannot exceed 45° degree, which makes the maximum value in radian as 0.785.

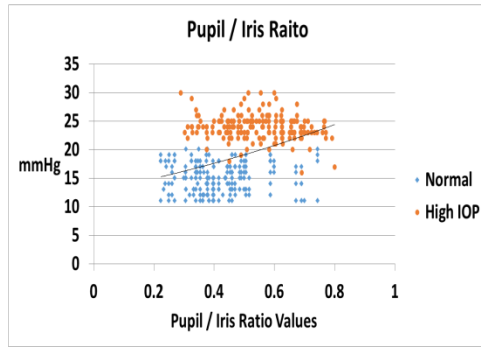


(a)

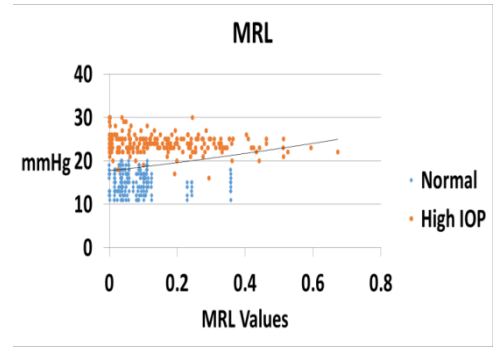


(b)

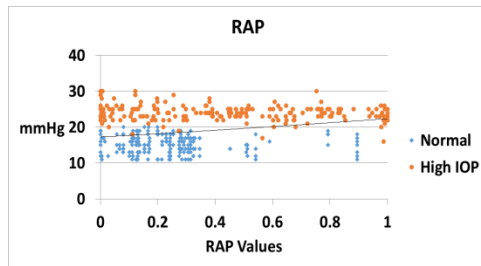
Figure 5.3 (a) Normal eye pressure (b) High IOP.



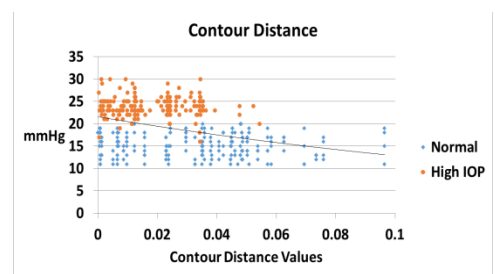
(a)



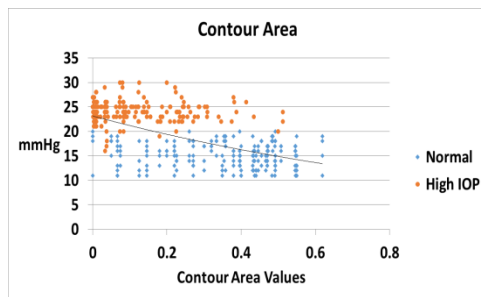
(b)



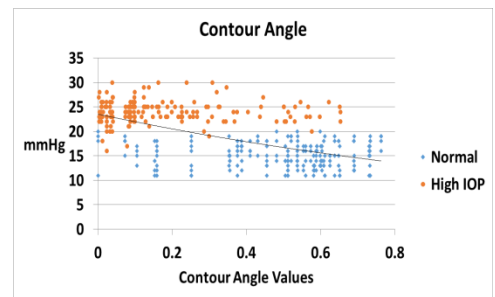
(c)



(d)



(e)



(f)

Figure 5.4 Correlation between normalized (a) Pupil/Iris Ratio feature, (b) Red Area Percentage feature, (c) Mean Redness Level feature, (d) Contour Distance feature, (e) Contour Area feature, and (f) Contour Angle feature, with IOP in mmHg.

5.3 Statistical Power Analysis

Moreover, to make sure that the utilized sample size is sufficient for testing; statistical power analysis is applied to confirm the accuracy claims for the two

experiments. For the first experiment, statistical power analysis is performed with the aim of estimating the minimum sample size to be used for the experiment.

To find out what the appropriate sample size would be or justify a proposed sample size, one would need to know the following factors [113].

- 1) Level of significant (p).
- 2) Effect size (d).

When considering an alpha level of 0.80 from Table 5.12, as a large set is used for the t-test on means calculation, the effect size will be “d”.

Table 5.12. Cohen Table of Statistical Power Analysis

	Effect Size index	Small	Medium	Large
<i>t-test on mean</i>	<i>d</i>	0.20	0.50	0.80
<i>t-test on correlation</i>	<i>r</i>	0.10	0.30	0.50
<i>F-test Anova</i>	<i>f</i>	0.10	0.25	0.40
<i>F-test regression</i>	<i>f²</i>	0.02	0.15	0.35
<i>Chi-Square Test</i>	<i>w</i>	0.10	0.30	0.50

In this work, with the anticipated effect size of $d=0.80$, desired statistical power level of 0.80 and probability level of 0.05, using the t-test of means:

$$\text{Minimum Sample size}(n) = \frac{N \times p(1-p)}{[N-1 \times (d^2 \div z^2)] + p(1-p)} \quad (5.6)$$

where $N=400$, $p=80\%$, $d=5\%$ and $z=1.96$, the sample size (n) can be calculated as:

$$n = (400 \times 0.8 \times (1-0.8)) / ((400-1) \times ((0.05^2) / (1.96^2)) + 0.8 \times (0.2)) = 152$$

The equation shows that the minimum sample size is 152. This is while the sample size that we are working on is 400 images, and more than sufficient to confirm the accuracy claims.

Another statistical power analysis has been applied for the second experiment to confirm that the sample size is sufficient and to verify the hypothesis claims for the improved segmentation accuracy of FCN over CHT. The main aim is to estimate the minimum sample size to be used for the experiments. The power of a statistical test is the probability that the test will reject the null hypothesis H_0 when the null hypothesis is false by confirming the alternative hypothesis H_1 when the alternative hypothesis is true. Therefore, two opposing hypotheses could be stated as follows:

$$H_0: \mu_A - \mu_B \leq \delta \quad (5.7)$$

$$H_1: \mu_A - \mu_B > \delta \quad (5.8)$$

where δ is the superiority or non-inferiority margin and the ratio between the sample sizes of the two groups is (also known as the matching ration):

$$k = \frac{n_A}{n_B} \quad (5.9)$$

The following formula has been used to calculate the sample size:

$$n_A = k \cdot n_B \quad (5.10)$$

$$n_B = \left(1 + \frac{1}{k}\right) \left(\sigma \frac{z_{1-\alpha} + z_{1-\beta}}{\mu_A - \mu_B - \delta}\right)^2 \quad (5.11)$$

$$1 - \beta = \theta(z - z_{1-\alpha}) + \theta(-z - z_{1-\alpha}) \quad (5.12)$$

$$z = \frac{\mu_A - \mu_B - \delta}{\sigma \cdot \sqrt{\frac{1}{n_A} + \frac{1}{n_B}}} \quad (5.13)$$

where σ is the standard deviation, θ is the standard normal distribution function, α is Type I error, β is Type II error (i.e. $1 - \beta$ is the power), and δ is the testing margin.

In this work, Group B corresponds to the mean segmentation error ' $\mu_B = 0.366$ ' for FCN and Group 'A' corresponds to the mean segmentation error ' $\mu_A = 0.535$ ' for CHT. The standard deviation ' $\sigma = 0.5$ ', the superior margin ' $\delta = 0.01$ ' and the sample ration ' $k = 1$ ' for the analysis. The final outcome from the statistical power analysis yields a minimum sample size of ' $n = 134$ '.

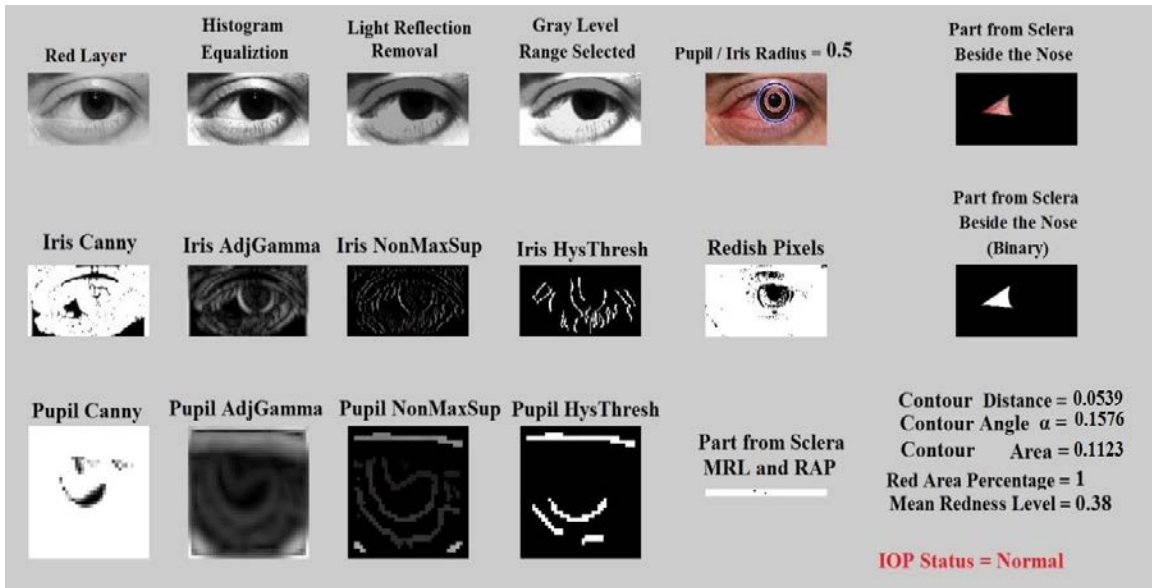
This shows that the minimum sample size required is 134. This is while the sample size that we are working on is a dataset of 400 images, plus additional images with more than 800 images overall. This is more than sufficient to confirm the accuracy claims that FCN results in less segmentation error compared to CHT.

5.4 Efficiency Test

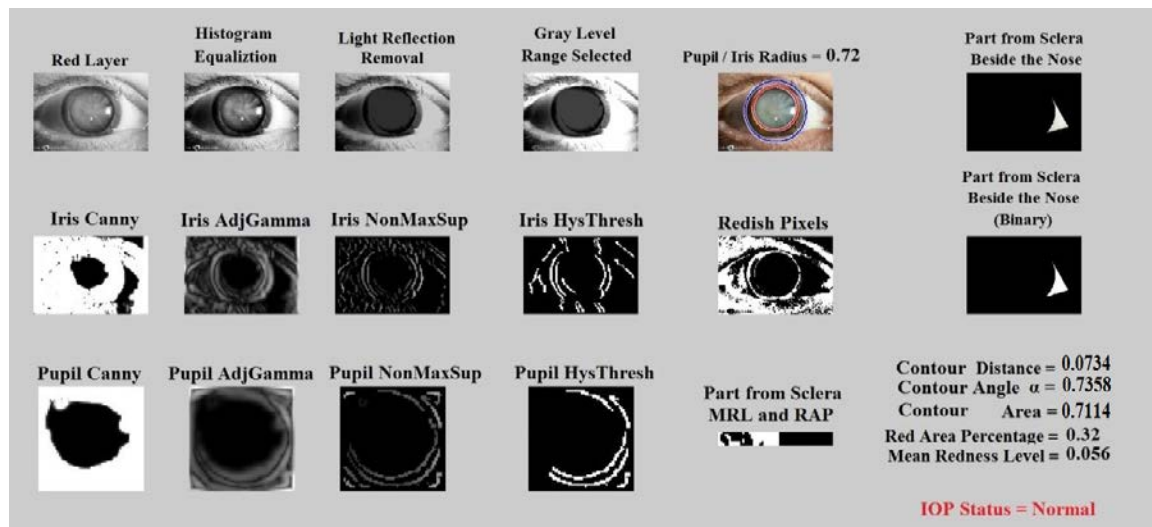
This framework has been created to help in the initial screening and risk assessment of IOP. However, the features that we count on to achieve our target may exist in other diseases like eye redness, and Cataract. Therefore, the framework has been

tested with eye images representing other diseases to see if the system is able to distinguish between IOP and other diseases.

To check the robustness of the proposed system, a test has been carried out on over additional 100 frontal eye images from different populations (diverse races and ages) with normal IOP, which have, however, been diagnosed with other eye diseases (Cataract, eye redness and trauma) [114, 115]. The system was able to extract the features correctly and as shown in the examples in Figures 5.5 (a and b), the tested samples have been correctly classified as normal IOP. This shows that the system is able to differentiate between IOP status and other diseases that share the same features.



(a)



(b)

Figure 5.5 (a) Red eye with Normal IOP (b) Cataract eye with Normal IOP.

CHAPTER 6: CONCLUSION AND FUTURE DIRECTIONS

In this dissertation, we have proposed a novel automated non-contact and non-invasive computer vision-based framework contributing to smart healthcare for analyzing frontal eye images to help in the early detection of high risk IOP. Image processing and machine learning techniques were used to assist in detecting high risk eye pressure cases.

The dataset used in this study included 200 normal eye pressure cases and 200 cases with high eye pressure. The proposed framework was implemented in MATLAB 2014a.

Two experiments were applied in this study. The first experiment includes five features: Pupil/Iris ratio, RAP, MRL, contour area and contour height. Sclera segmentation was derived by using the CHT technique in this experiment. The RAP, MRL and contour features were calculated by using the whole sclera. Once the features have been measured, two classification techniques (SVM, NN) were applied to train and test the images in order to detect the status of IOP. In the second experiment, six features were extracted from the frontal eye image: Pupil/Iris ratio, RAP, MRL, contour area, contour distance, and contour angle. Sclera segmentation in this experiment was derived by using the FCN technique. The RAP and MRL features were measured by using a rectangular region of interest from the sclera, where the contour features were calculated from a triangular region of interest from the sclera. Once the features have been

measured, two classification techniques (SVM, DT) were applied to train and test the images in order to detect the status of IOP.

In this study, the achieved framework provides a solid evidence of the relationship between the extracted features and IOP which has not been previously investigated through automated image processing and machine learning techniques on frontal eye images. This research was built on top of our preliminary data found in [101, 102] to assist clinicians and patients for early screening of IOP risk

As a future direction, more analysis will be provided to optimize the framework in terms of robustness and efficiency and investigate applying this work to mobile devices such as smartphones to make this work available and easily accessible to everyone. The framework can thus be used to check the patient's IOP status (normal or high) over time. The images and results can be further registered as a profile for each patient to identify if risky elevations of IOP have occurred.

Moreover, the framework can be further optimized to work on eye images taken from different angles. Despite showing promising results, some limitations exist. One concern is that the proposed features may not be the most optimum features to achieve the best accuracy. The efficiency of the proposed features can be investigated further in the future. In addition, to date, there is no publicly available dataset of frontal eye images annotated with IOP that researchers in the field can work on. Having access to or creating a much larger and comprehensive database with frontal eye images from diverse populations/conditions and investigating the efficiency and robustness of the proposed work is a future direction of this research. Nevertheless, this research provides

preliminary findings on the relationship between frontal eye image features and IOP using a reasonable size dataset and opens up avenues for further investigation. In the future, more frontal eye images including those from participants of several races can be fed to the image database. Additional tests and analysis can also be conducted so the framework can differentiate between IOP and other eye diseases like cataract and redness. Moreover, many core processors can be used to enhance the efficiency of the framework [106, 107]. Also the security and framework optimization can be added to the framework [116,117]

Another future direction of his research is to increase the features, rank, and then select a portion of the best ranked features that provides the highest sensitivity. In addition, the work can be extended to provide an output to users that is not binary (presence or absence of disease), and rather provide a score (e.g. between 0 to 1). This can be called “IOP Severity” in which the users will know the severity and progression of IOP, instead of presence or absence of high IOP. This can be achieved by using regression and multi-class classification models. For this, however, a database of images with timestamps of IOP progression labeled by ophthalmologist over time is needed.

REFERENCES

- [1] Salam A. A, Akram M. U, Wazir K, Anwar S. M. and Majid M. Autonomous Glaucoma detection from fundus image using cup to disc ratio and hybrid features. 2015 IEEE International Symposium on Signal Processing and Information Technology (ISSPIT), Abu Dhabi, 370:374. 2015.
- [2] Dutta M. K, Mourya A. K, Singh A, Parthasarathi M, Burget R. and Riha K. Glaucoma detection by segmenting the super pixels from fundus colour retinal images. Medical Imaging, m-Health and Emerging Communication Systems (MedCom), 2014 International Conference on, Greater Noida, 86:90, 2014.
- [3] Salam A. A., Akram M. U., Wazir K. and Anwar S. M. A review analysis on early Glaucoma detection using structural features. 2015 IEEE International Conference on Imaging Systems and Techniques (IST), Macau, 1:6, 2015.
- [4] Damon W. W. K., Liu J., Meng T. N., Fengshou Y. and Yin W. T. Automatic detection of the optic cup using vessel kinking in digital retinal fundus images, 2012 9th IEEE International Symposium on Biomedical Imaging (ISBI), Barcelona, 1647:1650, 2012.
- [5] Kinsey V. Comparative Chemistry of Aqueous Humor In Posterior And Anterior Chambers Of Rabbit Eye: Its Physiologic Significance. AMA Arch Ophthalmol, 50(4):401:417, 1953.

- [6] Manik G, Renata G, Richard K, and Sanjoy K. Aqueous Humor Dynamics: A Review. *The open othalamology journal*, Sep. 2010, 52:59.
- [7] Seiler T., Wollensak J. The resistance of the trabecular meshwork to aqueous humor outflow. *US National Library of Medicine, National Institutes of Health*, 1985, 88:91.
- [8] Darlene A et al. *Ocular Periphery and Disorders*. 2010. University of Alabama at Birmingham, 2010.
- [9] Mabuchi F, Yoshimura K, Kashiwagi K, Shioe K, Yamagata Z, Kanba S, Iijima H, Tsukahara S. High Prevalence of Anxiety and Depression in Patients With Primary Open-angle Glaucoma. *US National Library of Medicine National Institutes of Health*. Oct, 88:91, 2008.
- [10] Michal Schwartz. Vaccination for glaucoma: dream or reality?. *Brain Research Bulletin*. Volume 62, Issue 6, 15 February, 481:484, 2004.
- [11] Five Common Glaucoma Tests. (Glaucoma Research Foundation), <http://www.Glaucoma.org/Glaucoma/diagnostic-tests.php>. Accessed March 17, 2016.
- [12] M. Civana, AD. Macknightb. The ins and outs of aqueous humour secretion, *US National Library of Medicine National Institutes of Health*, pp. 88-91, Mar. 2014.
- [13] R.A. Moses, W. Grodzki, Jr., E. Etheridge, and C. Wilson. Schlemm's canal: the effect of intraocular pressure. *Investigative Ophthalmology and Visual Science*, pp. 61-68, Jan. 1981.
- [14] Leske, M. C. (1983). The epidemiology of open-angle glaucoma: a review. *American journal of epidemiology*, 118(2), 166-191, 1983.

- [15] J. Cheng et al., Focal edge association to glaucoma diagnosis, 2011 Annual International Conference of the IEEE Engineering in Medicine and Biology Society, Boston, MA, pp. 4481-4484, 2011.
- [16] Harry A. Open-Angle Glaucoma. *The New England Journal of Medicine*, vol. 328, no. 15, pp. 1097-1106 April, 1993.
- [17] M. Claro, L. Santos, W. Silva, F. AraUjo and A. Dalíia e Andre Santana, Automatic Detection of Glaucoma Using Disc Optic Segmentation and Feature Extraction, Computing Conference (CLEI), 2015 Latin American, Arequipa, , pp. 1-7, 2015.
- [18] Sorkhabi, R., Rahbani, M. B., Ahoor, M. H., & Manoochehri, V. (2012). Retinal Nerve Fiber Layer and Central Corneal Thickness in Patients with Exfoliation Syndrome. *Iranian Journal of Ophthalmology*, 24(2), 40-46, 2012.
- [19] Five Common Glaucoma Tests. (Glaucoma Research Foundation). Retrieved March 17, 2016, <http://www.glaucoma.org/glaucoma/diagnostic-tests.php>.
- [20] Nathan C, Fang W, James M. Issues in the epidemiology and population-based screening of primary angle-closure glaucoma. *Survey of Ophthalmology*, vol.36,no.6,pp. 411-423 May. 1992.
- [21] Saw, S. M., Gazzard, G., Friedman, D., Foster, P. J., Devereux, J. G., Wong, M. L., & Seah, S. (2003). Awareness of glaucoma, and health beliefs of patients suffering primary acute angle closure. *British journal of ophthalmology*, 87(4), 446-449, 2003.
- [22] Mabuchi F, Yoshimura K, Kashiwagi K, Shioe K, Yamagata Z, Kanba S, Iijima H, Tsukahara S, High Prevalence of Anxiety and Depression in Patients With Primary

- Open-angle Glaucoma, US National Library of Medicine National Institutes of Health, pp. 88-91, Oct. 2008.
- [23] Glaucoma and Traditional Chinese Medicine In China: <http://www.tcm-treatment.com/images/diseases/glaucoma.htm> [Accessed Aug. 4, 2018].
- [24] Healthy Eyes with Chinese Medicine: <https://www.acufinder.com/Acupuncture+Information/Detail/Healthy+Eyes+with+Chinese+Medicine> [Accessed Aug. 4, 2018].
- [25] L. Yuan and X. Xu, Adaptive Image Edge Detection Algorithm Based on Canny Operator, 2015 4th International Conference on Advanced Information Technology and Sensor Application (AITS), Harbin, pp. 28-31, 2015.
- [26] N. Ramakrishnan, M. Wu, S. K. Lam and T. Srikanthan, Automated thresholding for low-complexity corner detection, Adaptive Hardware and Systems (AHS), 2014 NASA/ESA Conference on, Leicester, pp. 97-103, 2014.
- [27] A. Mariakakis, E. Wang, S. Patel and J. C. Wen, A smartphone-based system for assessing intraocular pressure, 2016 38th Annual International Conference of the IEEE Engineering in Medicine and Biology Society (EMBC), Orlando, FL, pp. 4353-4356, 2016.
- [28] A. Posner, Modified conversion tables for the Maklakov tonometer, Eye. Ear. Nose Throat Mon., vol. 41, pp. 638–644, 1962.
- [29] C. Gisler, A. Ridi, M. Fauquex, D. Genoud and J. Hennebert, Towards glaucoma detection using intraocular pressure monitoring, 2014 6th International Conference of Soft Computing and Pattern Recognition (SoCPaR), Tunis, pp. 255-260, 2014.

- [30] Chih-Wei H., Chih-Chung C. and Chih-Jen L., A Practical Guide to Support Vector Classification, National Taiwan University, Taiwan, 2010, <http://www.csie.ntu.edu.tw/~cjlin>.
- [31] M. Shahiri-Tabarestani, B. A. Ganji and R. Sabbaghi-Nadooshan, Design and simulation of new micro-electromechanical pressure sensor for measuring intraocular pressure, 2012 16th IEEE Mediterranean Electrotechnical Conference, Yasmine Hammamet, pp. 208-211, 2012.
- [32] Yousefi S. et al. Learning From Data: Recognizing Glaucomatous Defect Patterns and Detecting Progression From Visual Field Measurements. in IEEE Transactions on Biomedical Engineering, Vol. 61, No. 7, 2112:2124, July 2014.
- [33] Yousefi S. et al. Glaucoma Progression Detection Using Structural Retinal Nerve Fiber Layer Measurements and Functional Visual Field Points. in IEEE Transactions on Biomedical Engineering, Vol. 61, No. 4, 1143:1154, April 2014.
- [34] Bendaoudi, H. Cheriet, F. Ben Tahar, H. Langlois, J.M.P., A scalable hardware architecture for retinal blood vessel detection in high resolution fundus images, in Design and Architectures for Signal and Image Processing (DASIP), 2014 Conference on , pp. 1-6, Oct. 2014.
- [35] Almi'ani, M.M. Barkana, B.D., A modified region growing based algorithm to vessel segmentation in magnetic resonance angiography, in Systems, Applications and Technology Conference (LISAT), 2015 IEEE Long Island, pp.1-7, May 2015.
- [36] Hassan, H. Azis, S.F.A., A simple approach of blood vessels detection in retinal images using MATLAB, in Research and Development (SCORED), 2012 IEEE Student Conference on, pp.245-249, Dec. 2012.

- [37] Sengar, N. Dutta, M.K. Parthasarathi, M. Burget, R., Extraction of retinal vasculature by using morphology in fundus images, in Signal Processing and Integrated Networks (SPIN), 2015 2nd International Conference on , pp.139-142, Feb. 2015.
- [38] Hernández, A.G.M., Image Analysis Algorithms for Feature Extraction in Eye Fundus Images, Universitat Autònoma de Barcelona (UAB), M.S Thesis, 2009.
- [39] Ruela Pereira Borges, V. Junqueira dos Santos, D. Popovic, B. Farias Cordeiro, D., Segmentation of Blood Vessels in Retinal Images Based on Nonlinear Filtering, in Computer-Based Medical Systems (CBMS), 2015 IEEE 28th International Symposium on, pp.95-96, June 2015.
- [40] M. M. Fraz, S. Barman, P. Remagnino, A. Hoppe, A. Basit, B. Uyyanonvara, A. R. Rudnicka, and C. G. Owen, An approach to localize the retinal blood vessels using bit planes and centerline detection, Computer methods and programs in biomedicine, vol. 108, no. 2, pp. 600–616, 2012.
- [41] Nikhil A. Yogesh B. Sharad C. and S.L.Tade. (2013). Retinal Blood Vessel Segmentation Algorithm for Diabetic Retinopathy and Abnormality Detection Using Image Substraction. International Journal of Advanced Research in Electrical, Electronics and Instrumentation Engineering. Vol. 2, Issue 4,pp. 1547-1553, 2013.
- [42] Luo G. Opas C. and Shankar M. K. (2002). Detection and Measurement of Retinal Vessels in Fundus Images Using Amplitude Modified Second-Order Gaussian Filter. IEEE Transactions on Biomedical Engineering, VOL. 49, NO. 2. pp 168-172, 2002.

- [43] Ana M. M., and Aurélio C. (2006). Segmentation of Retinal Blood Vessels by Combining the Detection of Centerlines and Morphological Reconstruction. IEEE Transactions on Medical Imaging, VOL. 25, NO. 9. pp 1200-1213, 2006.
- [44] OakarP., and AungSoe K. (2014). Automatic Detection of Optic Disc and Blood Vessels From Retinal Images Using Image Processing Techniques. IJRET: International Journal of Research in Engineering and Technology. pp 300-307, 2014.
- [45] Nidhal El A., and Enas Al S. (2014). Blood Vessel Diameter Measurement on Retinal Image. Journal of Computer Science 10 (5): Science Publications. pp 879-883, 2014.
- [46] SojuG., and Bhailal L. (2013). A Review Paper On Detection And Extraction Of Blood Vessels, Microaneurysms and Exudates From Fundus Images. International Journal of Scientific & Technology Research Volume 2, Issue 11, pp 191-206, 2013.
- [47] A. Osareh, and B. Shadgar. (2009). Automatic Blood Vessel Segmentation In Color Images of Retina. Iranian Journal of Science & Technology, Transaction B, Engineering, Vol. 33, No. B2, pp 191-206, 2009.
- [48] YashowardhanK., and Mohammed I. K. (2013). A Newly Rule-Based Method for Blood Vessel Segmentation –Multi-scale single-channel linear tracking method. Vol 4 (2), pp 369-373, 2013.
- [49] JaspreetK., and Dr. H.P.Sinha. (2012). Automated Detection of Retinal Blood Vessels in Diabetic Retinopathy Using Gabor Filter. IJCSNS International Journal of Computer Science and Network Security, VOL.12 No.4. pp 109-116, 2012.
- [50] Safia S. Anam T., and M. U. A. (2013). A Comparison and Evaluation of Computerized Methods for Blood Vessel Enhancement and Segmentation in Retinal

- Images. International Journal of Future Computer and Communication, Vol. 2, No. 6. pp. 600-603, 2013.
- [51] Reyhaneh S. Michael B. Susan A., and Chris T. (2010). Detection of Retinal Blood Vessels Using Complex Wavelet Transforms and Random Forest Classification. pp 1-5, 2010.
- [52] Lassada S. Bunyarit U., and Sarah B. (2005). Comparison of Edge Detection Techniques on Vessel Detection of Infant's Retinal Image. Proceedings of the International Conference on Computer and Industrial Management, ICIM, October 29-30, , Bangkok, Thailand. pp 61-65, 2005.
- [53] Joes S. Michael D. A. Meindert N. Max A. V, and Bram van G. (2004). Ridge-Based Vessel Segmentation in Color Images of the Retina. IEEE Transactions on Medical Imaging, VOL. 23, NO. 4. pp 501-509, 2004.
- [54] Patange, S. Jagadale, A., Framework for detection of cataract and gradation according to its severity, in Pervasive Computing (ICPC), 2015 International Conference on , pp.1-3, Jan. 2015.
- [55] K Hung Y Zhang, Preliminary investigation of Pupil size variability: toward non-contact assessment of cardiovascular variability, in Medical Devices and Biosensors, 2006. 3rd IEEE/EMBS International Summer School on, pp.137-140, Sep. 2006.
- [56] X. Long, Tonguz, O.K. Kidernan, A., Real Time Pupil Size Monitoring as a Screening Method for Diabetic Retinopathy, in Biomedical Circuits and Systems Conference, 2007. BIOCAS 2007. IEEE, pp.215-218, Nov. 2007.

- [57] Y. Du, E. Arslanturk, Z. Zhou and C. Belcher, Video-Based Noncooperative Iris Image Segmentation, in IEEE Transactions on Systems, Man, and Cybernetics, Part B (Cybernetics), vol. 41, no. 1, pp. 64-74, Feb. 2011.
- [58] Cullen, J. Fieguth, P. Pounder, S. Whitear, K., Analysis of corneal images for assessing contact lens trauma, in Image Processing, 2000. Proceedings. 2000 International Conference on, pp.176-179, 2000.
- [59] Raj Vardhan Azad, Devindra Sood Advances in the Management of Primary Adult Glaucomas, All India Ophthalmological Society, pp 1-67.
- [60] Umihira, Junichi, Seiji Nagata, Masahiko Nohara, Toru Hanai, Nobuteru Usuda, and Katsuzo Segawa. Localization of elastin in the normal and glaucomatous human trabecular meshwork. *Investigative Ophthalmology and Visual Science* 35 (1994): 486-486, 1994.
- [61] Murphy, Collin G., Mark Johnson, and Jorge A. Alvarado. Juxtacanalicular tissue in pigmentary and primary open angle glaucoma the hydrodynamic role of pigment and other constituents. *Archives of ophthalmology* 110, no. 12 (1992): 1779-1785, 1992.
- [62] Lee, A. J., E. Rohtchina, J. J. Wang, P. R. Healey, and P. Mitchell. Open-angle glaucoma and systemic thyroid disease in an older population: The Blue Mountains Eye Study. *Eye* 18, no. 6 600-608, 2004.
- [63] Johnson, M., and K. Erickson. Mechanisms and routes of aqueous humor drainage. *Principles and Practice of Ophthalmology*: 2577-2595, 2000.
- [64] Nakatake, Shunji, Shigeo Yoshida, Shintaro Nakao, Ryoichi Arita, Miho Yasuda, Takeshi Kita, Hiroshi Enaida, Yuji Ohshima, and Tatsuro Ishibashi. Hyphema is a

- risk factor for failure of trabeculectomy in neovascular glaucoma: a retrospective analysis. *BMC ophthalmology* 14, no. 1: 55, 2014.
- [65] Saccà, Sergio C., and Alberto Izzotti. *Oxidative Stress in Anterior Segment of Primary Open Angle Glaucoma*. INTECH Open Access Publisher, 2011.
- [66] Umihira, Junichi, Seiji Nagata, Masahiko Nohara, Toru Hanai, Nobuteru Usuda, and Katsuzo Segawa. Localization of elastin in the normal and glaucomatous human trabecular meshwork. *Investigative Ophthalmology and Visual Science* 35: 486-486, 1994.
- [67] Sihota, Ramanjit, Amita Goyal, Jasbir Kaur, Viney Gupta, and Tapas C. Nag. Scanning electron microscopy of the trabecular meshwork: understanding the pathogenesis of primary angle closure glaucoma. *Indian journal of ophthalmology* 60, no. 3: 183, 2012.
- [68] Benozzi, Jorge, Lucio P. Nahum, Julieta L. Campanelli, and Ruth E. Rosenstein. Effect of hyaluronic acid on intraocular pressure in rats. *Investigative ophthalmology & visual science* 43, no. 7: 2196-2200, 2002.
- [69] Lynch, Mary G., and Reay H. Brown. Stent device and method for treating glaucoma. U.S. Patent 6,464,724, issued October 15, 2002.
- [70] Strouthidis, Nicholas G., and Michael JA Girard. Altering the way the optic nerve head responds to intraocular pressure—a potential approach to glaucoma therapy. *Current opinion in pharmacology* 13, no. 1: 83-89, 2013.
- [71] Bhartiya, Shibal, Ritu Gadia, Harinder S. Sethi, and Anita Panda. Clinical Evaluation of Optic Nerve Head in Glaucoma. *Journal of Current Glaucoma Practice* 4, no. 3: 115-132, 2010.

- [72] Brodsky, Michael C. Congenital optic disc anomalies. In *Pediatric neuro-ophthalmology*, pp. 59-96. Springer New York, 2010.
- [73] Hitchings, R. A., and G. L. Spaeth. The optic disc in glaucoma II: correlation of the appearance of the optic disc with the visual field. *British Journal of Ophthalmology* 61, no. 2: 107-113, 1977.
- [74] Borchert, Mark, and Pamela Garcia-Filion. The syndrome of optic nerve hypoplasia. *Current neurology and neuroscience reports* 8, no. 5: 395-403, 2008.
- [75] American Academy of Optometry: Case Report 5, Clinical Findings and Management of Idiopathic Central Serous Chorioretinopathy.
- [76] Richard T. Libby, Douglas B. Gould, Michael G. Anderson, Simon W.M. COMPLEX GENETICS OF GLAUCOMA SUSCEPTIBILITY *John Annual Review of Genomics and Human Genetics* 6:1, 15-44, 2005.
- [77] Spoerl, Eberhard, Andreas G. Boehm, and Lutz E. Pillunat. The influence of various substances on the biomechanical behavior of lamina cribrosa and peripapillary sclera. *Investigative ophthalmology & visual science* 46, no. 4: 1286-1290, 2005.
- [78] Albon, Julie, Peter P. Purslow, Wojciech SS Karwatowski, and David L. Easty. Age related compliance of the lamina cribrosa in human eyes. *British Journal of Ophthalmology* 84, no. 3: 318-323, 2000.
- [79] Bhartiya, Shibal, Ritu Gadia, Harinder S. Sethi, and Anita Panda. Clinical Evaluation of Optic Nerve Head in Glaucoma. *Journal of Current Glaucoma Practice* 4, no. 3: 115-132, 2010.

- [80] Gong, Haiyan, Wen Ye, Thomas F. Freddo, and M. Rosario Hernandez. Hyaluronic acid in the normal and glaucomatous optic nerve. *Experimental eye research* 64, no. 4: 587-595, 1997.
- [81] Jung, Youn Hea, Hae-Young L. Park, Kyoung In Jung, and Chan Kee Park. Comparison of Prelaminar Thickness between Primary Open Angle Glaucoma and Normal Tension Glaucoma Patients. *PloS one* 10, no. 3, 2015.
- [82] Hernandez, M. R. Ultrastructural immunocytochemical analysis of elastin in the human lamina cribrosa. Changes in elastic fibers in primary open-angle glaucoma. *Investigative ophthalmology & visual science* 33, no. 10: 2891-2903, 1992.
- [83] Quigley, H. A., R. M. Hohman, E. M. Addicks, and W. R. Green. Blood vessels of the glaucomatous optic disc in experimental primate and human eyes. *Investigative ophthalmology & visual science* 25, no. 8: 918-931, 1984.
- [84] Hedges, Thomas R. Assessing the vascular supply of the optic disc. In *North American Neuro-ophthalmology Society Meeting, Rancho Mirage, California*, vol. 21. 2001.
- [85] Jia H., Zhang Y., Wang W., Xu J. Accelerating Viola-Jones Face Detection Algorithm on GPUs, *IEEE 9th International Conference on High Performance Computing and Communication, IEEE 14th International Conference on Embedded Software and Systems (HPCC-ICISS)*, 396:403, 2012.
- [86] Thompson A., The Cascading Haar Wavelet Algorithm for Computing the Walsh-Hadamard Transform, in *IEEE Signal Processing Letters*, vol. 24, no. 7, pp. 1020-1023, July 2017.

- [87] Chen J. J., Su C. R., Grimson W. E. L, Liu., J. L. and Shiue D. H. Object Segmentation of Database Images by Dual Multiscale Morphological Reconstructions and Retrieval Applications. in IEEE Transactions on Image Processing, vol. 21, no. 2, 828:843, 2012.
- [88] Raheja J., Sahu G. Pellet Size Distribution Using Circular Hough Transform in Simulink. American Journal of Signal Processing, Vol. 2 No. 6, 158:161, 2012.
- [89] Ramakrishnan N., Wu M., Lam S. K. and Srikanthan T. Automated thresholding for low-complexity corner detection. Adaptive Hardware and Systems (AHS), 2014 NASA/ESA Conference on, Leicester, 97:103, 2014.
- [90] Yuan L. and Xu X. Adaptive Image Edge Detection Algorithm Based on Canny Operator. 2015 4th International Conference on Advanced Information Technology and Sensor Application (AITS), Harbin, 28:31, 2015.
- [91] Basu M. Gaussian-based edge-detection methods-a survey. In IEEE Transactions on Systems, Man, and Cybernetics, Part C (Applications and Reviews), vol. 32, no. 3, 252:260, 2002.
- [92] Neubeck and Van L. Gool. Efficient Non-Maximum Suppression. 18th International Conference on Pattern Recognition (ICPR'06), Hong Kong, 850:855, 2006.
- [93] R. Medina-Carnicer, A. Carmona-Poyato, R. Muñoz-Salinas and F. J. Madrid-Cuevas, Determining Hysteresis Thresholds for Edge Detection by Combining the Advantages and Disadvantages of Thresholding Methods, in IEEE Transactions on Image Processing, vol. 19, no. 1, pp. 165-173, Jan. 2010.

- [94] Meer P. and Georgescu B. Edge detection with embedded confidence. in IEEE Transactions on Pattern Analysis and Machine Intelligence, vol. 23, no. 12, 1351:1365, Dec 2001.
- [95] Long, J., et al. (2014). Fully Convolutional Networks for Semantic Segmentation. CoRR abs/1411.4038.
- [96] Badrinarayanan, V., et al. (2015). SegNet: A Deep Convolutional Encoder-Decoder Architecture for Image Segmentation. CoRR abs/1511.00561.
- [97] Yu, F. and V. Koltun (2015). Multi-Scale Context Aggregation by Dilated Convolutions. CoRR abs/1511.07122, 2015.
- [98] Chen, L.-C., et al. (2016). DeepLab: Semantic Image Segmentation with Deep Convolutional Nets, Atrous Convolution, and Fully Connected CRFs. CoRR abs/1606.00915, 2016.
- [99] Peng, C., et al. (2017). Large Kernel Matters - Improve Semantic Segmentation by Global Convolutional Network. CoRR abs/1703.02719, 2017.
- [100] Borza, D., Darabant, A. S., and Danescu, R. Real-Time Detection and Measurement of Eye Features from Color Images. Sensors, PMC, 16(7), 1105, 2016.
- [101] Al-Oudat M., Faezipour M., and El-Sayed A. A smart intraocular pressure risk assessment framework using frontal eye image analysis. EURASIP Journal on Image and Video Processing, Vol. 1, 90, 2018.
- [102] Aloudat, M. Faezipour M El-Sayed, A., High Intraocular Pressure Detection from Frontal Eye Images: A Machine Learning Based Approach. accepted (to appear), IEEE Engineering in Medicine and Biology Conference (EMBC'18), 2018.

- [103] F. Leymarie and M. D. Levine. Tracking deformable objects in the plane using an active contour model. In *IEEE Transactions on Pattern Analysis and Machine Intelligence*, vol. 15, no. 6, pp. 617-634, 1993.
- [104] Ma XY, Zhu D, Zou J, Zhang WJ, Cao YL. Comparison of ultrasound biomicroscopy and spectral-domain anterior segment optical coherence tomography in evaluation of anterior segment after laser peripheral iridotomy. *Int J Ophthalmol*, 417:423, 2016.
- [105] Andrew B. et al, Active Contour. Department of engineering science, Springer, 1998.
- [106] C. Yan, H. Xie, D. Yang, J. Yin, Y. Zhang and Q. Dai, Supervised Hash Coding With Deep Neural Network for Environment Perception of Intelligent Vehicles. in *IEEE Transactions on Intelligent Transportation Systems*, vol. 19, no. 1, pp. 284-295, Jan. 2018.
- [107] C. Yan, H. Xie, S. Liu, J. Yin, Y. Zhang and Q. Dai. Effective Uyghur Language Text Detection in Complex Background Images for Traffic Prompt Identification. in *IEEE Transactions on Intelligent Transportation Systems*, vol. 19, no. 1, pp. 220-229, Jan. 2018.
- [108] Breiman, L., J. H. Friedman, R. A. Olshen, and C. J. Stone. Classification and Regression Trees. Boca Raton, FL: Chapman & Hall, 1984.
- [109] Walker H. K., Hall W. D., Hurst J. W. Clinical Methods: The History, Physical, and Laboratory Examinations. 3rd edition. Boston. 1990.

- [110] Sen, B., Peker, M., Çavuşoğlu, A., Çelebi, F.V. A comparative study on classification of sleep stage based on EEG signals using feature selection and classification algorithms. *J. Med. Syst*, 1:2, 2014.
- [111] Hassan, A.R. Bhuiyan, M.I.H. Computer-aided sleep staging using complete ensemble empirical mode decomposition with adaptive noise and bootstrap aggregating. *Biomed. Signal Process. Control*, 1:10, 2016.
- [112] Fraiwan, L. Lweesy, K. Khasawneh, N. Wenz, H. Dickhaus, H. Automated sleep stage identification system based on time–frequency analysis of a single EEG channel and random forest classifier. *Comput. Methods Progr. Biomed*, 10:19, 2012.
- [113] Cohen J., *Statistical power analysis for the behavioral sciences* (rev: Lawrence Erlbaum Associates, Inc, 1977).
- [114] Centre vision bretagne (2018). Cataract eye, Retrieved from: <http://www.centrevisionbretagne.com/ophtalmologuevannes/cataracte.php>.
- [115] Effective Home Remedies for Common Eye Problems (2018). Red eye sclera, Retrieved from <https://hubpages.com/health/Home-Remedies-for-Common-Eye-Problems>.
- [116] R. Abdulhammed, M. Faezipour and K. Elleithy. Malicious behavior monitoring of embedded medical devices. 2017 IEEE Long Island Systems, Applications and Technology Conference (LISAT), Farmingdale, NY, pp.1-6, 2017.
- [117] H. A. Musafir and A. Mahmood. Dynamic Hassan Nelder Mead with Simplex Free Selectivity for Unconstrained Optimization. in *IEEE Access*, vol. 6, pp. 39015-39026, 2018.